

# Seismic attenuation in Antarctic firn

Stefano Picotti<sup>1</sup>, José M. Carcione<sup>1,2</sup>, and Mauro Pavan<sup>3</sup>

<sup>1</sup>National Institute of Oceanography and Applied Geophysics (OGS), Trieste, Italy.

<sup>2</sup>School of Earth Sciences and Engineering, Hohai University, Nanjing, China.

<sup>3</sup>University of Genova, Italy.

**Correspondence:** Stefano Picotti (spicotti@ogs.it)

## Abstract.

We estimate the seismic attenuation of P- and S-waves in the polar firn and underlying ice by spectral analysis of diving, refracted, and reflected waves from active-source three-component seismic signals obtained in 2010 on the Whillans Ice Stream (WIS), a fast-flowing ice stream in West Antarctica. The resulting quality factors are then successfully modeled using a rock-physics theory of wave propagation that combines White's mesoscopic attenuation theory of interlayer flow with that of Biot/squirt flow. The first theory describes a viscoelastic medium equivalent of a stack of two alternating thin porous layers of thickness much greater than the pore size but smaller than the wavelength. On the other hand, in the so-called Biot/squirt-flow model, there are two loss mechanisms, namely the global Biot flow and the local flow from fluid-filled microcracks (or grain contacts) to the pore space and back, where the former is dominant over the latter. The fluid saturating the pores is assumed to be fluidized snow, defined as a mixture of snow particles and air, such as powder, having zero rigidity modulus.

## 1 Introduction

The shallow part of polar ice sheets and ice streams, commonly known as firn, is subjected to snow densification, a metamorphic process activated by the pressure gradient due to the accumulation of snow and by the temperature gradient at the near surface (Wilkinson, 1988). As a result, the density of firn increases continuously from the surface to the pore close-off depth, where the material has a density of about  $840 \text{ kg/m}^3$  and can be considered glacial ice (Herron and Langway, 1980). Below this depth, the compression of englacial bubbles further increases the ice density until the maximum value is reached. In the cold and dry internal parts of the Antarctic continent, the densification is slow and the firn layer thickness exceeds 100 m (van den Broeke, 2008). On the other hand, in the high-strain shear margins of ice streams, this metamorphic process can be enhanced due to the effect of strain softening (Oraschewski and Grinsted, 2022), leading to exceptionally thin firn layers.

Because of its density structure, polar firn is generally laterally homogeneous with the seismic velocity increasing non-linearly with depth. This velocity profile results in a continuous refraction of seismic waves (Greenhalgh and King, 1981), which are also called diving waves. There are many examples in the literature that used diving waves to estimate the firn velocity-depth structure by picking and inverting first-break traveltimes (e.g., Kirchner and Bentley, 1979; King and Jarvis, 2007; Picotti et al., 2015). The ice-fabric characteristics as a function of depth have been obtained by exploiting the P- and S-wave anisotropic velocities inferred from active-seismic surveys conducted in different settings (e.g., Blankenship and Bentley,

1987; Picotti et al., 2015). However, while tomographic methods for estimating seismic velocity in the whole ice column are well established, algorithms for quantifying the depth dependence of attenuation are underdeveloped. In particular, as far as we know, there are no examples of vertical profiling and modeling of the intrinsic seismic attenuation of P- and S-waves in the polar firn, so far.

30 Intrinsic loss is often quantified using the inverse quality factor  $1/Q$ , which represents the fraction of wave energy lost to heat in each wave period (e.g., Carcione, 2022; Gurevich and Carcione, 2022). P-wave quality factors ( $Q_P$ ) in ice have been measured by several authors in various depth ranges, from values as low as 5 in the temperate ice at the surface of mountain glaciers (e.g., Gusmeroli et al., 2010) up to 700 within cold polar ice caps (e.g., Bentley and Kohlen, 1976). This wide range of values indicates a strong dependence of the quality factor on temperature, demonstrated by laboratory experiments (e.g.,  
35 Kuroiwa, 1964). This dependence was also verified by Peters et al. (2012) from seismic measurements in Greenland, where  $Q_P$  decreases with depth due to an increase in temperature. In this case,  $Q_P$  was measured within narrow depth ranges, using strong basal and englacial reflections. Furthermore, it is common practice to measure the average  $Q_P$  over the entire ice column using the primary and multiple reflection events (e.g., Holland and Anandakrishnan, 2009; Booth et al., 2012). Regarding the S-wave quality factor ( $Q_S$ ), Cleve et al. (1969) and Carcione et al. (2021) measured  $Q_S$  in warm mountain glacier ice, reporting values  
40 of about 23 and 12, respectively. To our knowledge, no other measurements of  $Q_S$  in glacial ice or firn have been published in the literature.

While cold polar ice attenuation is low, this is not the case for polar firn. Bentley and Kohlen (1976) obtained a value of the ice  $Q_P$  from seismic refraction measurements at Byrd Station of about 715 at 136 Hz, between 100 m and 500 m depth and at an average temperature of about  $-28$  °C. Because this value is very high, intrinsic attenuation in polar ice (below the firn) is a  
45 minor factor in reducing the signal amplitude, in their case. On the other hand, Albert (1998) performed numerical simulations of seismic waves in firn at the South Pole, Antarctica, between 0 and 300 m, where he neglected seismic attenuation on the basis of Bentley and Kohlen's results. However, as we show in the present work, attenuation in firn cannot be neglected, since the  $Q_P$  factor has values between 4 and 50 down to 40 m depth, thus inducing a strong energy loss and velocity dispersion near the surface.

50 Regarding the attenuation mechanisms, Bentley and Kohlen (1976) assume that their results are "consistent with damping in slightly contaminated ice by a combination of two mechanisms: molecular relaxation at temperatures colder than about  $-20$  °C and grain boundary viscosity at warmer temperatures". However, their study does not provide a physical predictive micro-structural model for attenuation. Grain boundary relaxation and melting theories based on the Arrhenius equation can be important at temperatures close to the melting point of ice. In the case of rocks such a model has been applied to describe  
55 seismic attenuation at the crust and mantle (Carcione et al., 2018).

Here we consider three attenuation mechanisms based on physical models described in Pride et al. (2004), Carcione and Picotti (2006) and Carcione (2022). We show that wave-induced fluid flow generates enough heat to explain the levels of intrinsic attenuation. This flow occurs at different spatial scales that can broadly be categorized as "macroscopic", "mesoscopic" and "microscopic". The macroscopic flow is the wavelength-scale equilibration occurring between the peaks and troughs of a  
60 P wave. This mechanism was first treated by Biot (1956) and is simply referred to as "Biot loss". The microscopic flow occurs

when a wave squeezes a porous medium having grain contacts and cracks, which respond with a greater fluid pressure than the main pore space resulting in a flow from crack to pores, named "squirt flow". Finally, mesoscopic length scales are those much larger than grain sizes but smaller than wavelengths. Heterogeneity across these scales may be due to frame variations or to patches of different immiscible fluids. In our case, because of the seasonal alternation, the firn can be considered a finely layered medium consisting in the deposition of two porous media, one layer snow-like with high porosity and the other ice-like with low porosity (e.g., van den Broeke, 2008). When a compressional wave squeezes such a medium, the effect is similar to squirt with the more compliant portions of the material responding with a greater fluid pressure than the stiffer portions. What follows is a flow of fluid capable of generating significant loss in the seismic band. In the case of the Antarctic firn, the seismic wave attenuation cannot be explained by adopting a simple porous model consisting of a rigid structure of ice and a porous space filled with air. Such a simple ice-air model underestimates the seismic attenuation by orders of magnitude. Therefore, the fluid saturating the pore space in this case is assumed to be fluidized snow, a mixture of snow particles and air (Mellor, 1974; Maeno and Nishimura, 1979; Nishimura, 1996). In this study we demonstrate that the replacement of air with pore-fluidized snow leads to increased attenuation, and to quality factor values comparable with those obtained from seismic data. To our knowledge, this is the first attempt to use the concept of fluidized snow as a porous fluid in Biot's theory to model the wave attenuation in firn.

In the present work, we infer the P- and S-wave quality factor vertical profiles of the firn layer of Whillans Ice Stream (WIS – West Antarctica), using the three-component seismic data recorded on the Subglacial Lake Whillans (SLW), during the active-source experiment described in Horgan et al. (2012) and Picotti et al. (2015). First, we describe the data, the attenuation rock-physics theories and the methodology to extract the  $Q$  factor from the seismograms. Then, we analyze the spectral content of the diving-wave first breaks and refracted waves at the firn bottom, and compute the  $Q_P$  and  $Q_S$  factors using the frequency-shift technique. Finally, we fit the two vertical  $Q$  profiles using the presented rock-physics theories. In the discussion, we give a detailed explanation of the importance of this model for studies related to the physical properties of the firn and to the characterization of subglacial media using amplitude variations with offset (AVO) analysis (e.g., Peters et al., 2008, Booth et al., 2012). We describe an alternative procedure for calculating the average  $Q_P$  and  $Q_S$  of the ice column below the firn, using the reflected waves at the bottom of the glacier and the  $Q$  profile of the firn. This procedure can be useful in cases where conventional methods of amplitude preconditioning for AVO analysis are not applicable.

## 2 Seismic data

In the austral summer of 2010–2011, a comprehensive surface geophysics program surveyed a location on the WIS. The main target of the survey (Horgan et al., 2012; Christianson et al., 2012) was the seismic and radar characterization of the SLW (Fig. 1), an active subglacial lake that is the subject of a subglacial access program (Tulaczyk et al., 2014). Four active-source seismic profiles were acquired during this program: one profile parallel to the ice stream flow direction, following the long axis of the lake, and three transverse profiles across the lake (Fig. 1).

<< Figure 1 >>

Two types of seismic surveys were undertaken: one to obtain the characteristics of the firn and another for the imaging (Horgan et al., 2012) and to define the anisotropy of the whole ice column (Picotti et al., 2015). For the analysis of the velocity profile within the firn, a shallow-refraction dataset was generated using stacked hammer blows onto a wooden body embedded in the snow. This experiment is located on the longitudinal profile, as shown in Fig. 1. The data were recorded on a 48-channel seismic system using georods, consisting of five 40 Hz geophones wired in series (Voigt et al., 2013). The digital sample interval was 0.25 ms, and the maximum offset was 470 m, which is enough to define the velocity profile of the whole firn layer. To acquire the three components of the ground motion, the georods were rotated through the three mutually perpendicular axes. The horizontal longitudinal and transverse components are parallel and orthogonal to the profile, respectively. In the shallow-refraction survey, the trace spacing was increased with increasing offset to gain better resolution in the shallow part of the firn, which exhibits the strongest velocity gradient. The trace spacing is 1 m, 10 m and 20 m for offsets lower than 10 m, ranging between 10 and 290 m, and larger than 290 m, respectively. For the purposes of this work, generation and acquisition of S waves polarized in the orthogonal direction with respect to the seismic line (i.e., SH waves) is far better, because these are pure S waves, free of P-wave interferences. We also acquired the SV waves, polarized in the longitudinal vertical plane, but these signals are more affected by interferences from diving and multiple-refracted P-waves propagating in firn. The obtained seismograms are shown in Fig. 2, where the P and SH diving-wave first breaks picked for the traveltimes inversion and for the spectral analysis are indicated.

<< Figure 2 >>

All the other data (Fig. 1), aimed at defining the image and anisotropy of the entire ice column, were generated using 0.4 kg PETN (pentaerythritol tetranitrate) charges buried at a depth of 27 m using a hot water drill. Data were recorded on two 48-channel seismic systems and the sensors consisted of alternating single vertical 28 Hz geophones and georods spaced 20 m apart (Fig. 3a). In addition, multi-component data were acquired using three-component (3C) continuous recording stations (Fig. 3b). The 3C stations were first placed along the longitudinal profile, spaced 24 m apart and then moved to the transverse profiles, where the distance was 24 m and 240 m (Fig. 1). Each of these stations consisted of a Guralp 40-T broadband seismometer with 40 s corner period, coupled to a Reftek RT-130 data acquisition system equipped with GPS timing. The maximum offset was 4320 m for the data recorded using 3C stations and 1910 m for the other data. These data are described in more detail by Horgan et al. (2012) and Picotti et al. (2015).

<< Figure 3 >>

### 3 Theory and Methodology

#### 3.1 Theory overview

120 The theory of wave propagation in firm combines White's mesoscopic attenuation theory of interlayer flow (White et al., 1975; Carcione and Picotti, 2006; Carcione, 2022) and that of Biot/squirt flow (Gurevich et al., 2010; Carcione and Gurevich, 2011; Carcione, 2022). The first theory describes an equivalent viscoelastic medium of a stack of two thin alternating porous layers of thickness  $d_1$  and  $d_2$ , such that the period of the stratification is  $d = d_1 + d_2$ . The theory gives the complex and frequency dependent stiffness  $E$ , equivalent to the P-wave modulus. The complex velocity is given in Appendix A. On the other hand, in  
125 the so-called Biot/squirt-flow model, there are two loss mechanisms, namely the Biot global-flow one (Biot, 1956) and local flow from fluid-filled micro-cracks (or grain contacts) to the pore space and back. Fig. 4 shows a sketch of two sandstone grains in contact.

⟨⟨ Figure 4 ⟩⟩

Gurevich et al. (2010) assumed that a compliant pore forms a disk shaped gap between two grains and its edge opens into a toroidal stiff pore, where  $R$  is the radius of the contact (or crack) and  $h$  is its thickness. The model assumes that the material  
130 becomes stiffer when the fluid pressure does not have enough time to equilibrate between the stiff and compliant pores (grain contacts and main voids, respectively). To obtain the frequency-dependence of the stiffness moduli, the complex velocity is given in Appendix B.

#### 3.2 Phase velocity and quality factor

Denoting with  $v_1$ ,  $v_{2P}$  and  $v_{2S}$  the complex velocities corresponding to the mesoscopic (subscript 1) and Biot/squirt-flow  
135 (subscript 2) loss models, the global P-wave phase velocity and dissipation factor are

$$v_{pP} \approx v_{p2P} \tag{1}$$

and

$$\frac{1}{Q_P} = \frac{1}{Q_1} + \frac{1}{Q_{2P}}, \tag{2}$$

respectively, where

$$140 \quad v_{p2P} = \left[ \operatorname{Re} \left( \frac{1}{v_{2P}} \right) \right]^{-1} \tag{3}$$

and

$$Q_1 = \frac{\operatorname{Re}(v_1^2)}{\operatorname{Im}(v_1^2)}, \quad Q_{2P} = \frac{\operatorname{Re}(v_{2P}^2)}{\operatorname{Im}(v_{2P}^2)}. \tag{4}$$

Since the dominant mechanism is the Biot/squirt-flow one, we assume as a first approximation that the P-wave phase velocity is that of this loss mechanism. Alternatively, the phase velocity (1),  $v_{pP}(\omega)$ , can be obtained from  $Q_P(\omega)$  by using the Kramers-  
145 Kronig relations as given in Eq. (8) of Carcione et al. (2020) (see also Eq. (2.141) of Carcione, 2022).

Eq. (2) can be demonstrated if we consider that the decay factor along a distance  $r$  of a plane wave, due to the effect of the two attenuation mechanisms, is

$$\exp(-\alpha_1 r) \exp(-\alpha_{2P} r), \quad (5)$$

where  $\alpha$  are attenuation factors given by

$$150 \quad \alpha_1 = \frac{\pi f}{v_{p1} Q_1}, \quad \alpha_{2P} = \frac{\pi f}{v_{p2P} Q_{2P}}, \quad (6)$$

for low-loss media,  $v_{p1}$  is the mesoscopic-loss phase velocity and  $f$  is the frequency (see Eq. (2.129) in Carcione (2022)). Substituting (6) into (5), we obtain

$$\exp\left(-\frac{\pi f r}{v_{pP} Q_P}\right), \quad (7)$$

where we have assumed  $v_{p1} \approx v_{p2P}$ .

155 On the other hand, the properties of the S wave is solely described by the Biot/squirt-flow model, such that

$$v_{pS} = \left[ \operatorname{Re}\left(\frac{1}{v_{2S}}\right) \right]^{-1} \quad (8)$$

and

$$Q_S = \frac{\operatorname{Re}(v_{2S}^2)}{\operatorname{Im}(v_{2S}^2)}. \quad (9)$$

### 3.3 Estimation of the quality factor

160 To estimate the quality factor from the seismograms we adopted the frequency-shift method (e.g., Quan and Harris, 1997; Picotti and Carcione, 2006; Picotti et al., 2007). Let  $S(f)$  and  $R(f)$  be the amplitude quasi-Gaussian spectrums observed at the source and at a receiver, respectively, located at a mutual distance  $d$  in a homogeneous and isotropic medium. The frequency-shift approach is based on the property that, as the wave propagates through the medium, the high-frequency part of the spectrum decreases faster than the low-frequency part (Quan and Harris, 1997). This effect may be quantified by measuring  
165 the resulting downshift  $\Delta f = f_S - f_R$ , where  $f_S$  and  $f_R$  are the frequency centroids of  $S(f)$  and  $R(f)$ , respectively. Then, if we approximate the spectrum  $S(f)$  by a Gaussian with variance  $\sigma_S^2$ , we have

$$Q = \frac{\pi d \sigma_S^2}{v \Delta f} = \frac{\pi \Delta t \sigma_S^2}{\Delta f}, \quad (10)$$

where  $v$  is the velocity (P- or S-wave velocity), and  $\Delta t$  is the travelttime. Although this method is only applicable under the hypothesis of constant- $Q$  in the bandwidth of interest (Quan and Harris, 1997; Dasgupta and Clark, 1998), it can be applied with  
170 good reliability also to frequency-dependent  $Q$  media. For example, Picotti et al. (2007) estimated the frequency-dependent

$Q$  from numerically simulated seismograms by using the spectral-ratio and frequency-shift methods, finding values in good agreement with the synthetic theoretical models. Moreover, they found that the classical spectral-ratio method is more sensitive to this problem, resulting in noticeable departures of the logarithm of the spectral ratio from the linear trend. On the other hand, the frequency-shift method is less sensitive to this problem when the spectrum of the signal is Gaussian, because generally the
   
 175 quality factor variation is weak in the frequency band of active seismic experiments (typically 5-500 Hz). It becomes important only at the edges of the seismic frequency band where the integral contributions of the spectral amplitudes, for the calculation of the variances and of the frequency centroids, are negligible (e.g., Picotti and Carcione, 2006).

In the more general case of inhomogeneous media, the frequency shift along a raypath can be expressed as

$$\Delta f = \sigma_S^2 \int_{ray} \alpha_0 dl = \pi \sigma_S^2 \int_{ray} \frac{dl}{Qv}, \quad (11)$$

180 (Quan and Harris, 1997), where the integral is taken along the raypath and  $\alpha_0 = \pi/Qv$  is the attenuation factor, i.e., the attenuation coefficient is linearly proportional to frequency and defined as  $\alpha = \alpha_0 f$ . To infer the vertical  $Q$  profile of firm, we consider the whole firm column as a sequence of homogeneous- $Q$  layers. The  $Q$  of each individual layer is obtained adopting a layer-stripping method that considers the cumulative attenuation of all the overlying layers and exploits the monotonically increase of the firm's P- and S-wave velocities. The layer-stripping method is a well established technique both in traveltimes
   
 185 and attenuation tomography (e.g., Yilmaz, 2001; Böhm et al., 2006; Rossi et al., 2007). The P- and S-wave velocity fields (Fig. 5a) were previously computed in Picotti et al. (2015) by the traveltimes inversion of first arrivals, following the method of Herglotz and Wiechert (Herglotz, 1907; Wiechert, 1910; Nowack, 1990). This technique, applied for the first time to Antarctic seismic data by Kirchner and Bentley (1979), calculates the velocity-depth function from traveltimes-offset picked first-breaks. It is well suited to situations where the velocity increases monotonically with depth and for this reason it was successfully
   
 190 applied to firm by several authors (e.g., King and Jarvis, 2007). The resulting diving-wave paths in the velocity gradient (Fig. 5b) are obtained using an optimized ray-tracing algorithm based on the shooting method, described in Picotti et al. (2015). The curves displayed in Fig. 5a represent an improved version of those originally presented in Picotti et al. (2015).

⟨⟨ Figure 5 ⟩⟩

Let's consider a layer  $N$  in this succession, and assume the value of  $Q$  in the overlying  $N - 1$  layers to be already known. In our plane-layered model, the depth of each layer coincides with the depth of maximum penetration of each ray at increasing
   
 195 offsets. The ray corresponding to this layer reaches a receiver at the surface, whose recorded first-break frequency centroid is  $f_R$ . Under our hypothesis, and in accordance with Eq. (11), the total frequency shift occurred in the overlying  $N - 1$  layers is

$$\Delta f_{N-1} = 2 \sum_{i=1}^{N-1} \frac{\pi d_i \sigma_S^2}{v_i Q_i}, \quad (12)$$

where  $v_i$  and  $d_i$  are the velocities and the lengths of the ray segments in each layer, respectively, and the factor 2 accounts for both the downgoing and the upgoing wave. Then, the quality factor of the layer  $N$  is simply obtained by Eq. (10), where
   
 200  $d = d_N$ ,  $v = v_N$  and the frequency-shift in the layer  $N$  is given by  $\Delta f = \Delta f_N = f_S - f_R - \Delta f_{N-1}$ .

The layer-stripping method requires that the quality factor of the shallowest layer is known a priori. Moreover, the frequency centroid  $f_S$  and variance  $\sigma_S^2$  of the source must be known as well. These two values can be determined using the first breaks recorded by the receivers placed close to the source. To this purpose, it is necessary that the acquisition geometry is properly set to have a sufficient number of traces at very short offsets. Then, particular care must be devoted to acquire the first breaks with a high-quality of the signal, e.g., the wavelets must be free of interference effects and their amplitudes not clipped. If such type of signals are available, the following considerations allow for the computation of the required spectral properties. It is convenient in this case to use Eq. (10) to obtain the difference in the frequency content of propagating wavelets at different receivers. We consider the closest available signal to the source as reference wavelet, to be compared with the first breaks recorded at increasing offsets. In other words, we compare the spectrum  $R_1(f)$  of the reference wavelet to that of another wavelet  $R_2(f)$ , which propagates for an additional travelttime  $\Delta t$  in the same shallow layer. If the traces are sufficiently close to each other and to the source, it is possible to characterize the quality factor of the uppermost layer as the average of all calculated values, and the variance  $\sigma_S^2$  can be approximated to that of the reference wavelet. Finally, the dominant frequency of the source  $f_S$  follows from Eq. (10) by using the reference first-break travelttime.

## 4 Results

### 4.1 Quality factor vertical profiling

As previously described, a requirement for the layer-stripping technique is the knowledge of the quality factor of the shallowest layer, as well as the dominant frequency and variance of the source. We determined these properties by using the first breaks recorded close to the source, until a maximum offset of 10 and 6 m, for P and S waves, respectively.

Fig. 6 shows the time histories and the corresponding spectra of the considered P-wave first breaks.

<< Figure 6 >>

Unfortunately, the first breaks recorded at offsets lower than 7 m are contaminated by the SV waves, and the amplitudes very close to the source are clipped. Taking the signal recorded at 7 m offset as reference wavelet, we computed the frequency shifts and using Eq. (10) we estimated the average P-wave quality factor (and standard deviation) of the shallowest layer to be  $Q_P = 4.1 \pm 1.3$ . Calculating the maximum penetration depth of the ray emerging at 10 m offset, we estimated the thickness of this layer to be about 2.7 m. Moreover, the estimated source dominant frequency and variance are  $f_S = 574$  Hz and  $\sigma_S = 171$  Hz, respectively.

Fig. 7 shows the wavelets and the corresponding spectra of the considered S-wave first breaks.

<< Figure 7 >>



Because the amplitudes of the first break recorded at 1 m offset are clipped, this trace cannot be used as the reference. Taking the signal recorded at 2 m offset as reference wavelet, we computed the frequency shifts and using Eq. (10) we estimated the average S-wave quality factor (and standard deviation) of the shallowest layer to be  $Q_S = 1.9 \pm 0.4$ . By calculating the maximum penetration depth of the emerging ray at an offset of 6 m, we estimated the thickness of this layer to be about 1.6 m. Furthermore, the estimated dominant frequency and variance of the source are  $f_S = 496$  Hz and  $\sigma_S = 146$  Hz, respectively.

The frequency centroids of the diving P- and S-wave first-breaks are obtained from the spectra of the selected waveforms, as described in Picotti and Carcione (2006). The amplitude integrals are calculated, for each wavelet, in a frequency band from zero to the maximum frequency of the signal. Since this high cut-off frequency depends on the signal-to-noise ratio, a statistic is performed to evaluate the dispersion due to noise. The mean values of the obtained distributions of the frequency centroids, for both the first P- and S-wave breaks, are shown in Fig. 8. The corresponding standard deviations are less than 3 Hz. Both curves show a rapid decrease in the dominant frequency of the signal as a function of offset, except an increase in frequency for the P-waves between 10 and 30 m offset, which is an effect due to the diving waves travelling in that strong velocity- $Q$  gradient.

<< Figure 8 >>

As described above, the P- and S-wave velocity fields were previously computed in Picotti et al. (2015) by the traveltimes inversion of first arrivals, following the method of Herglotz and Wiechert (Herglotz, 1907; Wiechert, 1910; Nowack, 1990). The velocity curves shown in Fig. 5a represent an improved version of those originally presented in Picotti et al. (2015). The uncertainties in the velocities are obtained by perturbing the first-break travel times, according to the dominant frequency of the selected wavelets, and then repeating the Herglotz-Wiechert inversion to obtain different velocity distributions as a function of depth. The average and standard deviation of the obtained distributions are displayed in Fig. 5a. The maximum P- and S-wave velocities, verified using the first arrivals refracted at distant offsets on the seismograms acquired using the explosive source, are  $3864 \pm 30$  m/s and  $1947 \pm 25$  m/s at  $60 \pm 5$  m depth, respectively. At short offsets, errors increase due to the steep velocity gradient near the surface.

The two frequency curves shown in Fig. 8, the velocity profiles, the characteristics of the spectral source and  $Q_P$  and  $Q_S$  of the most superficial layer, are the inputs of the layer-stripping procedure, to calculate the P- and S-wave quality factor profiles of the entire firn column. The uncertainties in  $Q_P$  and  $Q_S$  profiles are obtained by repeating the procedure using the previously calculated frequency centroid and velocity distributions and perturbing the quality factors of the most superficial layers by their standard deviations. Then, from the two  $Q$ -factor distributions in output, we have derived the corresponding mean and standard deviation profiles with respect to depth.

Fig. 9 and Fig. 10 display the resulting  $Q_P$  and  $Q_S$  profiles for the whole firn column, from the surface to the ice, together with the dominant frequency computed at the maximum penetration depth of each diving raypath.

<< Figure 9 >>

<< Figure 10 >>

The first plot (Fig. 9) shows a gradual increase of  $Q_P$  from the previously computed minimum value of  $4.1 \pm 1.3$  close to the surface, to a value of  $120 \pm 35$  at about 50 m depth. Then, it increases sharply to over  $300 \pm 140$  at about 58 m depth. A noticeable increase of uncertainty below 40 m depth is due to a consistent reduction of traveltime and frequency shift in each layer. The second graph (Fig. 10) shows a moderate increase of  $Q_S$ , from the previously calculated minimum value of  $1.9 \pm 0.4$  near the surface, to an average maximum value of about  $250 \pm 90$ , which remains almost constant at depths greater than about 40 m.

Since the offset range is not sufficient to appreciate where the  $Q_P$  factor stabilizes at the maximum value in the ice, we used the dataset acquired with the explosive charges placed at 27 m depth (Fig. 3a), to analyze the refracted P-wave first breaks recorded at large offsets, until the maximum available offset of 1910 m. Fig. 11 shows an example of selected wavelets and the corresponding spectra, together with a reference wavelet recorded at 670 m offset. All these signals travel along similar raypaths in the firm, while their paths in the underlying ice have different lengths. Following the same principle adopted for the computation of the  $Q$  factor in the shallowest layer, we compare the spectrum of the reference wavelet to those of other wavelets that propagate for additional traveltimes in the deep ice. Because these paths through the ice are long, a difference in spectral centroids can be better appreciated and quality factors can be calculated more reliably. This procedure should be repeated for a large number of selected wavelets, in order to perform a statistical analysis. In this case, the average P-wave quality factor of the ice is  $Q_P = 380 \pm 70$  at  $60 \pm 5$  m depth, where the average measured temperature is about  $-24^\circ\text{C}$  (Engelhardt and Kamb, 1993). Using the same procedure, we also analyzed the refracted S-wave first breaks from 330 to 470 m offset (Fig. 2b and Fig. 8), resulting in an average ice S-wave quality factor of  $Q_S = 260 \pm 80$  at  $60 \pm 5$  m depth. This value confirms the result provided by the analysis of the diving waves.

<< Figure 11 >>

## 4.2 Modeling of the seismic properties of the firm

Firm is assumed to be a deposition of two porous media, one layer snow-like with high porosity and the other ice-like with low porosity. The grains (ice) have the properties  $K_s = 10$  GPa,  $\mu_s = 5$  GPa (shear modulus) and  $\rho_s = 917$  kg/m<sup>3</sup> in both layers (Gurevich and Carcione, 2022). The fluid saturating the pores is assumed to be fluidized snow, which is defined as a mixture of snow particles and air, like powder, having zero rigidity modulus. We consider  $K_f = 571$  MPa,  $\rho_f = 200$  kg/m<sup>3</sup> and  $\eta = 0.1$  Pa s. The properties of this material have been investigated by Mellor (1974), Maeno and Nishimura (1979) and Nishimura (1996).

For this study it is important to measure the properties of the fluidized phase of the snow. This task can be performed in coring of firm samples as indicated in Nishimura (1991). The main apparatus consists of two parts: fluidized snow feeder and inclined

285 chute, where it is possible to store the disintegrated snow in fluidized conditions. Measurements are made at a temperature of  
 –15 °C to avoid adhesion effects between snow particles. In this context, bulk density, elastic velocity and viscosity can be  
 measured.

The physical properties of the firn layer are obtained from the density model using functions of porosity that have been shown  
 to be suitable for snow. The density profile as a function of depth is obtained by using the following empirical relationship  
 290 (Kohnen, 1972):

$$\rho(z) = 0.917 \left[ 1 + \left( \frac{V_{P,ice} - V_P(z)}{2250} \right)^{1.22} \right]^{-1}, \quad (13)$$

where  $V_P(z)$  is the vertical P-wave velocity displayed in Fig. 5a, and  $V_{P,ice} = 3864$  m/s is the velocity in ice, which we assume  
 equal to the maximum computed P-wave velocity.

The porosity obtained from the experimental density (13) is

$$295 \quad \phi(z) = \frac{\rho_s - \rho(z)}{\rho_s - \rho_f}. \quad (14)$$

Fig. 12 shows the experimental density and porosity, where the former increase and the latter decrease monotonically with  
 depth, mainly due to compaction.

⟨⟨ Figure 12 ⟩⟩

Then, for each layer, the dry-rock bulk modulus which best fits the data of Johnson (1982) is

$$K_m = K_s (1 - \phi)^{30.85/(7.76 - \phi)}. \quad (15)$$

300 The dry-rock shear modulus is

$$\mu = \frac{3}{2} \frac{1 - 2\nu}{1 + \nu} K_m, \quad \nu = 0.38 - 0.36\phi, \quad (16)$$

where  $\nu$  is the Poisson ratio. Below the pore close-off depth, approximately 35 m in this case, the medium is mainly ice ( $\rho \geq$   
 840 kg/m<sup>3</sup> and  $\phi \leq 10$  %), and the Poisson ratio is better approximated from the inverted wave velocities as follows

$$\nu = \frac{V_P^2 - 2V_S^2}{2(V_P^2 - V_S^2)} \approx 0.32, \quad (17)$$

305 (Mavko et al., 2009), where  $V_P$  and  $V_S$  are the P- and S-wave velocities displayed in Fig. 5a, respectively.

The permeability is

$$\kappa = \frac{C}{\rho_s^2} \cdot \frac{\phi^3}{(1 - \phi)^2} \quad (18)$$

(Sidler, 2015; Gurevich and Carcione, 2023), where  $C = 0.012 \text{ kg}^2/\text{m}^4$  and we consider that the porosity  $\phi$  is obtained from the experimental velocities and density as given by Eqs. (13) and (14).

310 For the mesoscopic-loss model, we assume  $\phi_1(z) \approx \phi(z)$ ,  $p_1 = p_2 = 0.5$  and  $\phi_2 = \gamma\phi_1$ , where  $\gamma$  is small, i.e., layer 2 (ice) has a much lower porosity than layer 1 (snow). Here we assume  $\gamma = 0.1$ . On the other hand, the squirt-flow model has the following values of the parameters (Carcione and Gurevich, 2011):  $h/R = 0.015$ ,  $\phi_c = 0.0002$ ,  $K_h = 1.38K_m$ , where  $K_m$  is the bulk modulus with the grain contacts and cracks open. The attenuation is due to the softer layer with much higher porosity, since the cracks are open and the global-flow loss (Biot) mechanism is effective. The contribution of the stiff layer is negligible.

315 Fig. 13 shows the P- and S-wave velocities and dissipation factors as a function of frequency close to the surface, where  $\phi_1 = 0.744$ ,  $\phi_2 = 0.0744$ , and the solid and fluid properties of the two layers are the same. We can see that the dominant mechanism is the Biot (global-flow) one (Biot, 1956), with a strong relaxation peak (high attenuation) and velocity dispersion. The squirt-flow peak is weaker and located at lower frequencies, while the mesoscopic loss contributes only to the P wave. The P- and S-wave dissipation peaks occur at a frequency of approximately 282 Hz. On the other hand, the model predicts that

320 below a given depth (from 40 to 50 m) the squirt-flow loss predominates over the Biot global one.

<< Figure 13 >>

Let us now study the dependence of attenuation as a function of depth. We consider a frequency of 282 Hz, corresponding to the dissipation peaks in Fig. 13. Fig. 14a shows the comparison between the experimental and theoretical quality factor profiles as a function of depth, while Fig. 14b shows the  $Q_P$  and  $Q_S$  experimental errors. As expected, the uncertainties increase with increasing quality factor, in agreement with the fact that the attenuation effect weakens with increasing  $Q$ , and can be observed

325 with high accuracy only over large distances. The differences between the theoretical quality factor and the profiled  $Q$  are within the experimental errors almost for the entire firn column.

<< Figure 14 >>

## 5 Discussion

Studying the structure of polar ice sheets and basal materials is essential for modeling the response of ice masses to climate change. The mechanisms of basal movement of glaciers, which strongly influence the mass balance of Antarctica, are poorly

330 understood. The presence at the ice bottom of enormous quantities of water-saturated sediments, ponds and subglacial lakes, determines the dynamics of the ice streams (e.g., Bindshadler et al., 2003; Winberry et al., 2009), which represent the main drainage conduits of ice from the interior of Antarctica to the ocean. Furthermore, the identification and characterization of

subglacial lakes is also important for studying the climate history of Antarctica, including the possible presence of extremophile life (Siegert et al., 2011).

335 Seismic reflection techniques are powerful tools for mapping the physical properties of subglacial environments, specifically, roughness at the subglacial boundary, water occurrence and fluid layer thickness, rock and sediment type, sediment porosity and fluid saturation, thickness of the subglacial sedimentary layer (e.g., Blankenship et al., 1987). These parameters are all crucial for understanding the basal flow mechanism, which is modulated by the subglacial hydrology and deformation characteristics of the subglacial till. Seismic imaging is the only way to map these properties over large areas, as drilling to the ice bottom is  
340 extremely expensive and only provides local information.

The application of advanced AVO techniques has successfully exploited detailed tomographic velocity models and reflection amplitudes at the basal boundary to gather considerable information on the underlying material properties in various contexts (e.g., Blankenship et al., 1987; Anandakrishnan, 2003; Peters et al., 2008; Booth et al., 2012). However, quantitative estimates of these subglacial properties are difficult due to the many challenges that characterize AVO techniques. The two most important  
345 limitations are that the source characteristics are often unknown and that the attenuation of P and S waves can be highly variable vertically, across the entire ice column (and in some cases also laterally) and poorly constrained. Both of these conditions reduce the ability to quantify bedrock reflection coefficients, affecting uncertainties about the physical properties of subglacial materials.

Our method allows for a better understanding of the seismic properties of the firn, which are useful for estimating ice-sheet  
350 mass balance from satellite observations of ice-sheet elevation (e.g., Wingham, 2000; Alley et al., 2007). As explained, being  $Q$  strongly influenced by the porosity (and density) profile of the propagation medium, measuring both velocities and quality factors has the potential to provide additional information on the physical structure of the firn, avoiding costly coring.

Furthermore, the present work provides alternative means to correct for seismic reflection amplitudes at the glacier floor and can be very useful in cases where conventional amplitude preconditioning methods for AVO analysis are impossible. Indeed,  
355 conventional methods ignore the complex  $Q$  structure of the firn, and usually rely on the presence of multiple reflections to calculate the source amplitude and average quality factor of the entire ice column at normal incidence (e.g., Holland and Anandakrishnan, 2009; Booth et al., 2012). In addition to the fact that multiple reflections are not always present in seismic data, when available they often show a poor signal-to-noise ratio (e.g., Dow et al., 2013). In the case considered in this work, there is no evidence of multiple reflections in the overall data set. Therefore, the obtained firn velocity- $Q$  profile can help in  
360 calculating both the source amplitude and the average quality factor of the ice mass below the firn.

Consider an explosive charge buried deep in the firn (in our case about 27 m for most shots), and a ray propagating from the source to a surface receiver. Adopting our layered firn model, the source amplitude can be calculated considering the first breaks and the Eq. (7), expressing the decay factor along a distance  $r_i$  in each homogeneous layer. Neglecting the transmission loss between adjacent quasi-layers, and indicating with  $\alpha_i = \pi/Q_i v_i$  the attenuation factor in the layer  $i$ , the total amplitude of  
365 the source  $S(f)$  is

$$S(f) = GR(f) \prod_{i=1}^N \exp(\alpha_i f r_i) = GR(f) A_c(f), \quad (19)$$

where  $A_c(f)$  is the amplitude correction factor,  $f$  is the dominant frequency,  $N$  is the number of crossed layers,  $R(f)$  is the receiver amplitude and  $G$  takes into account frequency-independent factors, for example the geometric spreading factor, which is proportional to the total length of the ray. To reduce the uncertainty, the Eq. (19) can be applied to a large number of receivers  
 370 for each shot, in order to perform a statistical analysis.

Let us now consider the amplitude  $R(f)$  of a signal reflected from the bottom of the glacier. The reflection coefficient  $R_c$  is obtained by correcting  $R(f)$  for the decay factor as

$$R_c(f) = \frac{GR(f)A_c(f)}{S(f)}, \quad (20)$$

where the calculation of  $A_c(f)$  is now performed along the rays reflected from the bed. Therefore, this calculation implies  
 375 knowledge of the quality factor profile of the entire ice column. In this case, in the absence of englacial reflections, the average quality factor between the firn bottom and the bed is required. This value can be estimated, both for P and S waves, following the same principle adopted for the calculation of the  $Q$  factor in the most superficial layer (direct waves at short offsets) and at the base of the firn (refracted waves at large offsets). This method does not require a priori knowledge of the source characteristics, but only of the firn  $Q$  profile. We compare the spectrum of a reference wavelet with those of other wavelets  
 380 propagating further travel times in both firn and deep ice. For this purpose, we select a reference wavelet at a short offset (ray A) and another wavelet at large offset (ray B), as shown in Fig. 15. These signals travel along raypaths of slight dissimilar length in the firn, while their paths in the underlying ice have very different lengths. The greater the difference between the lengths of these paths, the larger the difference in the centroids of the spectrum and the greater the reliability of the calculated quality factor.

<< Figure 15 >>

385 Applying Eq. (11) to rays A and B we obtain

$$\sum_{rayB} \frac{\Delta t_k}{Q_k} - \sum_{rayA} \frac{\Delta t_k}{Q_k} = \frac{\Delta f_{BA}}{\pi \sigma_A^2}, \quad (21)$$

where  $\Delta f_{BA}$  is the difference between the frequency centroids of the reflected wavelets recorded at the receivers  $R_B$  and  $R_A$  (Fig. 15). Separating the contributions of ice and firn in the summations, the average quality factor of the ice mass below the firn is

$$390 \quad Q_{ice} = \frac{\sum_{rayB}^{ice} \Delta t_k - \sum_{rayA}^{ice} \Delta t_k}{\frac{\Delta f_{BA}}{\pi \sigma_A^2} - \left( \sum_{rayB}^{firn} \frac{\Delta t_k}{Q_k} - \sum_{rayA}^{firn} \frac{\Delta t_k}{Q_k} \right)} \quad (22)$$

<< Figure 16 >>

In the same way we estimated the ice quality factor using the waves refracted at the bottom of the firn, we adopted the dataset acquired with the explosive charges placed at a depth of 27 m (Fig. 3) in order to analyze the reflected waves from the glacier bottom. Fig. 16 and Fig. 17 show two examples of selected wavelets and corresponding spectra, up to maximum offset values of 1910 m and 2892 m for P and S waves, respectively. These are the largest offsets available in our dataset, showing signals with sufficient quality, in terms of signal-to-noise ratio. We performed a ray tracing adopting the algorithm described in Picotti et al. (2015), which allows to calculate the ice velocity versus propagation angle. Then, using the wavelet frequency centroids, the firn quality factor profiles, and calculated travel times along the ray segments, we obtained the average ice quality factors below the firn (both for P and S waves) using Eq. (22). This procedure should be repeated for a large number of selected wavelets, in order to perform a statistical analysis. In this case, the mean P-wave quality factor of the ice (and standard deviation) is  $Q_P = 320 \pm 60$ . Using the same procedure, we also analyzed the reflected S waves (Fig. 3b), obtaining an average ice quality factor of  $Q_S = 205 \pm 50$ . These values agree with the result provided by the diving and refracted waves. However, this analysis shows a slight decrease in ice quality factors, compared to the maximum values estimated at the bottom of the firn. This decrease reflects the substantial dependence of the quality factor on temperature (e.g., Kuroiwa, 1964; Peters et al., 2012), which increases with respect to depth in polar ice sheets and ice streams. In our case, in the SLW site the temperature increases from a minimum value of about  $-25^\circ\text{C}$  (annual mean temperature) near the surface, to a maximum value at the bed which is close to its pressure-melting point (Engelhardt and Kamb, 1993; Tulaczyk et al., 2014).

## 6 Conclusions

A physical explanation of the seismic attenuation (quality factor) in the polar snow and ice masses is essential to gaining insight into the ice sheet and deeper geological formations. This study shows a novel approach, based on a physical model depending on parameters that can be derived from core sample analyses, to interpret and explain the observed seismic wave attenuation in firn and in the underlying ice. In particular, the proposed model is useful for performing data processing and amplitude variations with offset inversions (AVOs), to extract basal petrophysical properties from active-source multichannel seismic data.

In this work we estimated the P- and S-wave attenuation profiles in the firn and underlying ice of Whillans Ice Stream (West Antarctica), from the spectral analysis of diving, refracted and reflected waves of active-source three-component seismic data. The resulting experimental quality factors range from values lower than 5 at the surface to approximately 300 and 250 at about 60 m depth, for P and S waves, respectively. Thus, the P wave quality factor further increases up to a maximum value of about 380 in the underlying ice. This attenuation model allowed us to infer the average quality factors of the P and S waves of the entire ice column beneath the firn, up to the bed, which is otherwise not possible using standard methods. The estimated average  $Q$  factors are slightly lower than the maximum values at the firn bottom, in agreement with the increase in temperature as a function of depth typical of the polar ice caps.

The firm wave propagation model combines White's mesoscopic attenuation theory of interlayer flow with that of Biot/squirt flow, and the fluid saturating the pores is assumed to be fluidized snow. The dominant attenuation mechanism is found to be that of the global Biot flow, with the theory showing good agreement with the experimental values for the whole firm column. 425 The model also predicts that below the pore close-off depth (approximately 35 m in this case) the squirt-flow loss predominates over the global Biot loss.

The proposed model allows to interconnect seismic experiments with mechanical laboratory analyses of firm samples collected on a study site, allowing for both calibration of seismic surveys and inversion of firm properties. To this aim, knowledge of both seismic velocity and attenuation is also important because they could allow, at least theoretically, to obtain the porosity 430 (and density) profile of the polar firm by means of surface or borehole seismic experiments, useful for estimating the ice-sheet mass balance from satellite observations of ice-sheet elevation. In light of this information, surface seismic experiments or well logging in inexpensive hot-water drilled holes could replace costly core drills.

### Appendix A: Mesoscopic-loss model

The complex P-wave modulus of two periodic thin porous layers is (White et al., 1975; Carcione, 2022)

$$435 \quad E = \left[ \frac{1}{E_0} + \frac{2(r_2 - r_1)^2}{i\omega(d_1 + d_2)(I_1 + I_2)} \right]^{-1}. \quad (\text{A1})$$

where

$$E_0 = \left( \frac{p_1}{E_{G1}} + \frac{p_2}{E_{G2}} \right)^{-1}, \quad (\text{A2})$$

with  $p_l = d_l / (d_1 + d_2)$ ,  $l = 1, 2$ ,

$$r = \frac{\alpha M}{E_G} \quad (\text{A3})$$

$$440 \quad I = \frac{\eta}{\kappa a} \coth\left(\frac{ad}{2}\right), \quad a = \sqrt{\frac{i\omega\eta E_G}{\kappa M E_m}}, \quad (\text{A4})$$

for each single layer,  $\omega$  is the angular frequency and  $i = \sqrt{-1}$ .

For each layer

$$E_m = K_m + \frac{4}{3}\mu \quad (\text{A5})$$

445 is the dry-rock P-wave modulus, being  $K_m$  and  $\mu$  the respective bulk and shear moduli,

$$E_G = E_m + \alpha^2 M \quad (\text{A6})$$

is Gassmann's P-wave modulus,

$$K_G = K_m + \alpha^2 M, \quad (\text{A7})$$



is Gassmann's bulk modulus,

$$450 \quad \alpha = 1 - \frac{K_m}{K_s}, \quad M = \left( \frac{\alpha - \phi}{K_s} + \frac{\phi}{K_f} \right)^{-1}, \quad (\text{A8})$$

where  $\phi$ ,  $K_s$  and  $K_f$  denote the porosity, and the bulk moduli of the grains and saturant fluid, respectively. The coefficient  $\alpha$  is known as the effective stress coefficient of the bulk material. Finally,  $\eta$  is the fluid viscosity and  $\kappa$  is the frame permeability.

Let  $\rho_s$  and  $\rho_f$  denote the mass densities of the grains and fluid, respectively, and let

$$\rho = (1 - \phi)\rho_s + \phi\rho_f \quad (\text{A9})$$

455 denote the mass density of the bulk material.

The complex velocity is

$$v_1 = \sqrt{\frac{E}{\rho}}. \quad (\text{A10})$$

This model considers only the P-wave attenuation, since the shear modulus  $\mu$  is real.

## Appendix B: Biot/squirt-flow model

460 The squirt-flow proelasticity stiffnesses are the Gassmann bulk and shear moduli,

$$K_G = K_m + \alpha(K_m)^2 M(K_m) \quad \text{and} \quad \mu_G = \mu_m \quad (\text{B1})$$

where

$$\alpha(K_m) = 1 - \frac{K_m}{K_s} \quad \text{and} \quad M(K_m) = \frac{K_s}{1 - \phi - K_m/K_s + \phi K_s/K_f}, \quad (\text{B2})$$

465  $\phi$  is the porosity,  $K_m$  and  $\mu_m$  are the bulk and shear moduli of the drained matrix, and  $K_s$  and  $K_f$  are the solid and fluid bulk moduli, respectively. We explicitly indicate the functional form of  $\alpha$  and  $M$  on  $K_m$ , since we shall replace this modulus by a modified matrix (or frame) complex modulus  $K$ , which includes the squirt-flow mechanism. In the same manner,  $\mu_m$  will be replaced by  $\mu$ . The new moduli are complex-valued and frequency-dependent.

In the Biot/squirt-flow model, the bulk and shear moduli of the saturated rock at low frequencies are given by Gassmann's equations,

$$470 \quad K_G = \bar{K} + \alpha^2(\bar{K})M(\bar{K}) \quad \text{and} \quad \mu_G = \bar{\mu}, \quad (\text{B3})$$

where  $\bar{K}$  and  $\bar{\mu}$  are the bulk and shear moduli of the modified frame including the un-relaxation due to the presence of the squirt-flow mechanism, and  $\alpha$  and  $M$  are given by Eq. (B2) substituting  $K_m$  with  $K$ . For simplicity, we keep the same notation for the Gassmann moduli, but now they are complex-valued and frequency-dependent.

Gurevich et al. (2010) obtained the modified dry moduli in the following form

$$\frac{1}{\bar{K}} = \frac{1}{K_h} + \left[ \left( \frac{1}{K_m} - \frac{1}{K_h} \right)^{-1} + \left( \frac{1}{K_f^*} - \frac{1}{K_s} \right)^{-1} \phi_c^{-1} \right]^{-1}, \quad (B4)$$

$$\frac{1}{\bar{\mu}} = \frac{1}{\mu_m} - \frac{4}{15} \left( \frac{1}{K_m} - \frac{1}{\bar{K}} \right),$$

where  $K_m$  and  $\mu_m$  are the dry-rock bulk and shear moduli at the confining pressure  $p_c$ ,  $K_h$  is the dry-rock bulk modulus at a confining pressure where all the compliant pores are closed, i.e., an hypothetical rock without the soft porosity, and  $\phi_c$  is the compliant porosity. This is so small – nearly 0.001 for most rocks – that the total porosity  $\phi$  can be assumed to be equal to the stiff porosity. The key quantity in Eqs. (B4) is the effective bulk modulus of the fluid saturating the soft pores:

$$K_f^* = \left[ 1 - \frac{2J_1(kR)}{kR J_0(kR)} \right] K_f, \quad k = \frac{2}{h} \sqrt{-\frac{3i\omega\eta}{K_f}} = \frac{1}{R} \sqrt{\frac{-8K_f^*}{K_f}}, \quad (B5)$$

where  $J_0$  and  $J_1$  are Bessel functions.

The complex velocities of the P and S waves are

$$v_{2P} = \sqrt{\frac{\bar{K} + 4\bar{\mu}/3}{\rho}} \quad (B6)$$

and

$$v_{2S} = \sqrt{\frac{\bar{\mu}}{\rho}}, \quad (B7)$$

respectively.

*Data availability.* The data presented in this work is available through the following previous publications: Horgan et al. (2012) and Picotti et al. (2015).

*Author contributions.* SP mainly conceived the study, processed and analyzed all data, produced most of the figures and wrote the manuscript.

490 SP and MP designed the experiment and acquired the seismic data in Antarctica. JMC contributed the basic ideas, proposing the theoretical models, producing some of the figures and writing several part of the text. All authors discussed the results and were involved in drafting the manuscript.

*Competing interests.* The contact author has declared that none of the authors has any competing interests.

*Acknowledgements.* This work was supported by the Italian National Program of Antarctic Research (PNRA–WISSLAKE Project) and the  
495 U.S. National Science Foundation (WISSARD Program–NSF 0944794, 0632198, and 0424589). We would like to thank Huw J. Horgan and  
Sridhar Anandakrishnan for their support.

## References

- Albert, D. G.: Theoretical modeling of seismic noise propagation in firn at the South Pole, Antarctica, *Geophys. Res. Lett.*, 25(23), 4257–4260, <https://doi.org/10.1029/1998GL900155>, 1998.
- 500 Alley, R. B., Spencer, M. K., and Anandakrishnan, S.: Ice-sheet mass balance: assessment, attribution and prognosis, *Annals of Glaciology*, 46, 1–7, <https://doi.org/10.3189/172756407782871738>, 2007.
- Anandakrishnan, S.: Dilatant till layer near the onset of streaming flow of Ice Stream C, West Antarctica, determined by AVO (amplitude vs  
505 offset) analysis, *Ann. Glaciol.*, 36, 283–286, <https://doi.org/10.3189/172756403781816329>, 2003.
- van den Broeke, M.: Depth and Density of the Antarctic Firn Layer. *Arctic, Antarctic, and Alpine Research*, 40(2), 432–438, [https://doi.org/10.1657/1523-0430\(07-021\)\[BROEKE\]2.0.CO;2](https://doi.org/10.1657/1523-0430(07-021)[BROEKE]2.0.CO;2), 2008.
- 510 Bentley, C. R. and Kohnen, H.: Seismic refraction measurements of internal friction in Antarctic ice, *J. Geophys. Res.*, 81, 1519–1526, <https://doi.org/10.1029/JB081i008p01519>, 1976.
- Bindschadler, R. A., King, M. A., Alley, R. B., Anandakrishnan, S., and Padman, L.: Tidally controlled stick-slip discharge of a West  
515 Antarctic ice stream, *Science*, 301, 1087–1089, <https://doi.org/10.1126/science.1087231>, 2003.
- Biot, M. A.: Theory of propagation of elastic waves in a fluid-saturated porous solid. I. Low frequency range, *J. Acoust. Soc. Am.*, 28(2), 168–178, <https://doi.org/10.1121/1.1908239>, 1956.
- Böhm, G., Accaino, F., Rossi, G., and Tinivella, U.: Tomographic joint inversion of first arrivals in a real case from Saudi Arabia,  
520 *Geophysical Prospecting*, 54, 721 – 730, <https://doi.org/10.1111/j.1365-2478.2006.00563.x>, 2006.
- Blankenship, D. D., Bentley, C. R., Rooney, S. T., and Alley, R. B.: Till beneath Ice Stream B. 1. Properties derived from seismic travel  
times, *J. Geophys. Res.*, 92(B9), 8903–8911, <https://doi.org/10.1029/JB092iB09p08903>, 1987.
- 525 Blankenship, D. D. and Bentley, C. R.: The crystalline fabric of polar ice sheets inferred from seismic anisotropy, in: *The Physical Basis of Ice Sheet Modelling*, (Proceedings of the Vancouver symposium, August 1987), IAHS Publ. 170, 17–28, 1987.
- Booth, A. D., Clark, R. A., Kulesa, B., Murray, T., Carter, J., Doyle, S., and Hubbard, A.: Thin-layer effects in glaciological seismic  
amplitude-versus-angle (AVA) analysis: implications for characterising a subglacial till unit, Russell Glacier, West Greenland, *The*  
530 *Cryosphere*, 6(4), 909–922, <https://doi.org/10.5194/tc-6-909-2012>, 2012.

- Carcione, J. M.: *Wave Fields in Real Media. Theory and numerical simulation of wave propagation in anisotropic, anelastic, porous and electromagnetic media*, Elsevier (Fourth edition, extended and revised), 2022.
- 535 Carcione, J. M., Gei, D., Picotti, S., and Botelho, M. A. B.: On the instantaneous frequency and quality factor. *Geophysical Journal International*, 227(2), 735–745, <https://doi.org/10.1093/gji/ggab250>, 2021.
- Carcione, J. M., Gei, D., Santos, J. E., Fu, L.-Y., and Ba, J.: Canonical analytical solutions of wave-induced thermoelastic attenuation, *Geophys. J. Int.*, 221, 835–842, <https://doi.org/10.1093/gji/ggaa033>, 2020.
- 540 Carcione, J. M. and Gurevich, B.: Differential form and numerical implementation of Biot’s poroelasticity equations with squirt dissipation, *Geophysics*, 76, N55–N64, <https://doi.org/10.1190/geo2010-0169.1>, 2011.
- Carcione, J. M., Poletto, F., Farina, B., and Bellezza, C.: 3D seismic modeling in geothermal reservoirs with a distribution of steam patch sizes, permeabilities and saturations, including ductility of the rock frame, *Physics of the Earth and Planetary Interiors*, 279, 67–78, <https://doi.org/10.1016/j.pepi.2018.03.004>, 2018.
- 545 Carcione, J. M. and Picotti, S.: P-wave seismic attenuation by slow-wave diffusion: Effects of inhomogeneous rock properties, *Geophysics*, 71, O1–O8, <https://doi.org/10.1190/1.2194512>, 2006.
- 550 Christianson, K., Jacobel, R. W., Horgan, H. J., Anandakrishnan, S., and Alley, R. B.: Subglacial Lake Whillans – Ice-penetrating radar and GPS observations of a shallow active reservoir beneath a West Antarctic ice stream, *Earth and Planetary Science Letters*, 331–332, 237–245, <https://doi.org/10.1016/j.epsl.2012.03.013>, 2012.
- 555 Clee, T. E., Savage, J. C., and Neave, K. G.: Internal friction in ice near its melting point, *J. Geophys. Res.*, 74(4), 973–980, <https://doi.org/10.1029/JB074i004p00973>, 1969.
- Dasgupta, R. and Clark, R. A.: Estimation of  $Q$  from surface seismic reflection data: *Geophysics*, 63(6), 2120–2128, <https://doi.org/10.1190/1.1444505>, 1998.
- 560 Dow, C., Hubbard, A., Booth, A., Doyle, S., Gusmeroli, A., and Kulesa, B.: Seismic evidence of mechanically weak sediments underlying russell glacier, west greenland, *Annals of Glaciology*, 54(64), 135–141, <https://doi.org/10.3189/2013AoG64A032>, 2013.
- Engelhardt, H. and Kamb, B.: Vertical temperature profile of Ice Stream B, *Antarctic J. US*, 28(5), 63–66, 1993.
- 565 Greenhalgh, S. A. and King, D. W.: Curved raypath interpretation of seismic refraction data, *Geophysical Prospecting*, 29(6), 853–882, <https://doi.org/10.1111/j.1365-2478.1981.tb01031.x>, 1981.

- 570 Gurevich, B. and Carcione, J. M.: Attenuation and dispersion of elastic waves in porous rocks: Mechanisms and models, SEG publication, 26, <https://doi.org/10.1190/1.9781560803911.fm>, 2022.
- Gurevich, B., Makarynska, D., de Paula, O., and Pervukhina, M.: A simple model for squirt-flow dispersion and attenuation in fluid-saturated granular rocks, *Geophysics*, 75, N109–N120, <https://doi.org/10.1190/1.3509782>, 2010.
- 575 Gusmeroli, A., Clark, R. A., Murray, T., Booth, A. D., Kullessa, B., and Barrett, B. E.: Seismic wave attenuation in the uppermost glacier ice of Storglaciären, Sweden, *Journal of Glaciology*, 56(196), 249–256, <https://doi.org/10.3189/002214310791968485>, 2010.
- Herglotz, G.: Über das Benndorfsche Problem der Fortpflanzungsgeschwindigkeit der Erdbebenstrahlen, *Physikal, Zeitschr. für Geophys.*, 8, 145–147, 1907.
- 580 Herron, M. M. and Langway, C. C.: Firn densification, an empirical model, *Journal of Glaciology*, 25, 373–385, <https://doi.org/10.3189/S0022143000015239>, 1980.
- Holland, C. and Anandkrishnan, S.: Subglacial seismic reflection strategies when source amplitude and medium attenuation are poorly known, *Journal of Glaciology*, 55(193), 931–937, <https://doi.org/10.3189/002214309790152528>, 2009.
- 585 Horgan, H. J., Anandkrishnan, S., Christianson, K., Jacobel, R. W., Alley, R. B., Heeszel, D. S., Picotti, S., and Jacob I. W.: Subglacial Lake Whillans – Seismic observations of a shallow active reservoir beneath a West Antarctic ice stream, *Earth and Planetary Science Letters*, 331–332, 201–209, <https://doi.org/10.1016/j.epsl.2012.02.023>, 2012.
- 590 Johnson, J. B.: On the application of Biot’s theory to acoustic wave propagation in snow, *Cold Regions Science and Technology*, 6, 49–60, [https://doi.org/10.1016/0165-232X\(82\)90044-1](https://doi.org/10.1016/0165-232X(82)90044-1), 1982.
- King, E. C. and Jarvis, E. P.: Use of shear waves to measure Poisson’s ratio in polar firn, *Journal of Environmental and Engineering Geophysics*, 12(1), 15–21, <https://doi.org/10.2113/JEEG12.1.15>, 2007.
- 595 Kirchner, J. F. and Bentley, C. R.: Seismic short refraction studies on the Ross Ice Shelf, Antarctica, *Journal of Glaciology*, 24(90), 313–319, <https://doi.org/10.3189/S0022143000014830>, 1979.
- 600 Kohnen, H.: On the relation between seismic velocities and density in firn and ice, *Z. Geophys.*, 38, 925–935, 1972.
- Kuroiwa, D. : Internal friction of ice. III : The internal friction of natural glacier ice. *Contributions from the Institute of Low Temperature Science*, 18, 49–62, 1964.

- 605 Maeno, N. and Nishimura, K.: Fluidization of snow, *Cold Reg. Sci. Technol.*, 1, 109–120, [https://doi.org/10.1016/0165-232X\(79\)90004-1](https://doi.org/10.1016/0165-232X(79)90004-1), 1979.
- Mavko, G., Mukerji, T. and Dvorkin, J.: *The rock physics handbook: tools for seismic analysis in porous media*, Cambridge Univ. Press, <https://doi.org/10.1017/CBO9780511626753>, 2009.
- 610 Mellor, M.: *A review of basic snow mechanics*, U.S. Army Cold Regions Research and Engineering Laboratory, 1974.
- Nishimura, K.: *Studies on the fluidized snow dynamics. Contributions from the Institute of Low Temperature Science, Ser. A, No. 37*, pp. 1-55 (Doctor Thesis, Hokkaido University), 1991.
- 615 Nishimura, K.: Viscosity of fluidized snow, *Cold Regions Science and Technology*, 24, 117–127, [https://doi.org/10.1016/0165-232X\(95\)00023-5](https://doi.org/10.1016/0165-232X(95)00023-5), 1996.
- Nowack, R. L.: Tomography and the Herglotz-Wiechert inverse formulation, *Pure and Applied Geophysics*, 133, 305–315, <https://doi.org/10.1007/BF00877165>, 1990.
- 620 Oraschewski, F. M. and Grinsted, A.: Modeling enhanced firn densification due to strain softening, *The Cryosphere*, 16, 2683–2700, <https://doi.org/10.5194/tc-16-2683-2022>, 2022.
- 625 Peters, L. E., Anandakrishnan, S., Alley, R. B. and Voigt, D. E.: Seismic attenuation in glacial ice: A proxy for englacial temperature, *J. Geophys. Res.*, 117, F02008, <https://doi.org/10.1029/2011JF002201D>, 2012.
- Peters, L. E., Anandakrishnan, S., Holland, C. W., Horgan, H. J., Blankenship, D. D., and Voigt, D. E. : Seismic detection of a subglacial lake near the South Pole, Antarctica, *Geophysical Research Letters*, 35(23), L23501, <https://doi.org/10.1029/2008GL035704>, 2008.
- 630 Picotti, S. and Carcione, J. M.: Estimating seismic attenuation ( $Q$ ) in the presence of random noise, *Journal of Seismic Exploration*, 15(2), 165–181, 2006.
- Picotti, S., Carcione, J. M., Rubino, J. G., and Santos, J. E.: P-wave seismic attenuation by slow-wave diffusion: Numerical experiments in partially saturated rocks, *Geophysics*, 72 (4), N11–N21, <https://doi.org/10.1190/1.2740666>, 2007.
- 635 Picotti, S., Vuan, A., Carcione, J. M., Horgan, H. J., and Anandakrishnan, S.: Anisotropy and crystalline fabric of Whillans Ice Stream (West Antarctica) inferred from multicomponent seismic data, *J. Geophys. Res. Solid Earth*, 120, 4237–4262, <https://doi.org/10.1002/2014JB011591>, 2015.
- 640

- Pride, S. R., Berryman, J. G., and Harris, J. M.: Seismic attenuation due to wave-induced flow, *J. Geophys. Res.*, 109, B01201, <https://doi.org/10.1029/2003JB002639>, 2004.
- 645 Quan, Y. and Harris, J. M.: Seismic attenuation tomography using the frequency shift method, *Geophysics*, 62, 895–905, <https://doi.org/10.1190/1.1444197>, 1997.
- Rossi, G., Gei, D., Böhm, G., Madrussani, G., and Carcione, J. M.: Attenuation tomography: An application to gas-hydrate and free-gas detection, *Geophysical Prospecting*, 55, 655–669, <https://doi.org/10.1111/j.1365-2478.2007.00646.x>, 2007.
- 650 Sidler, R.: A porosity-based Biot model for acoustic waves in snow, *Journal of Glaciology*, 61, 789–797, <https://doi.org/10.3189/2015JoG15J040>, 2015.
- Siegert, M., Kennicutt, M., Bindschadler, R.: Antarctic Subglacial Aquatic Environments. *Geophys. Monogr. Ser.*, vol. 192, <https://doi.org/10.1029/GM192>, 2011.
- 655 Tulaczyk, S., Mikucki, J., Siegfried, M., Priscu, J., Barcheck, C., Beem, L., and The Wissard Science Team: WISSARD at Subglacial Lake Whillans, West Antarctica: Scientific operations and initial observations, *Annals of Glaciology*, 55(65), 51–58, <https://doi.org/10.3189/2014AoG65A009>, 2014.
- 660 Voigt, D. E., Peters, L. E., and Anandkrishnan, S.: 'Georods': The development of a four-element geophone for improved seismic imaging of glaciers and ice sheets, *Annals of Glaciology*, 54(64), 142–148, <https://doi.org/10.3189/2013AoG64A432>, 2013.
- White, J. E., Mikhaylova, N. G., and Lyakhovitskiy, F. M.: Low-frequency seismic waves in fluid saturated layered rocks, *Physics of the Solid Earth*, 11, 654–659, 1975.
- 665 Wiechert, E.: Bestimmung des weges von erdbebenwellen, I. Theoretisches. *Phys. Z.*, 11, 294-304, 1910.
- Wilkinson, D. S.: A pressure-sintering model for the densification of polar firn and glacier ice, *Journal of Glaciology*, 34, 40–45, <https://doi.org/10.3189/S0022143000009047>, 1988.
- 670 Winberry, J. P., Anandkrishnan, S., Alley, R. B., Bindschadler, R. A., and King, M. A. : Basal mechanics of ice streams: Insights from the stick-slip motion of Whillans Ice Stream, West Antarctica, *Journal of Geophysical Research*, 114, F01016, <https://doi.org/10.1029/2008JF001035>, 2009.
- 675 Wingham D. J.: Small fluctuations in the density and thickness of a dry firn column, *Journal of Glaciology*, 478 46(154), 399–411, <https://doi.org/10.3189/172756500781833089>, 2000.



Yilmaz, O.: Seismic data analysis: processing, inversion and interpretation of seismic data, SEG Series: Investigation in Geophysics, Tulsa, <https://doi.org/10.1190/1.9781560801580>, 2001.

680

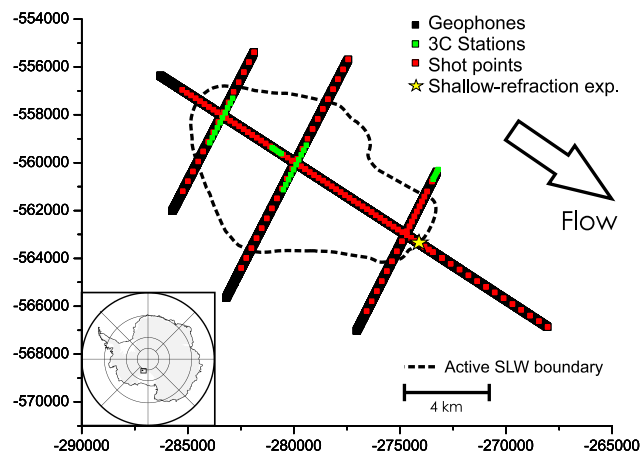


**Figure 1.** Map showing the location of SLW and the survey profile geometry (modified from Picotti et al., 2015). The location of the shallow-refraction experiment is indicated. Polar stereographic projection with true scale at  $-71^\circ$ .

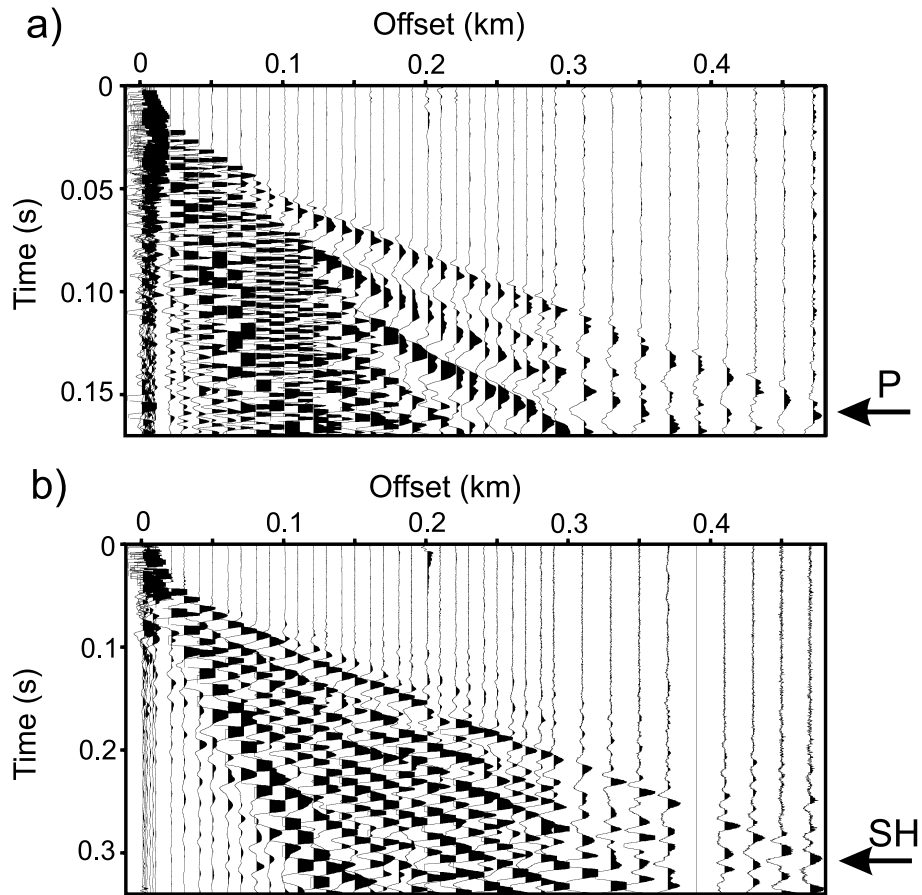


**Figure 2.** Hammer shallow-refraction seismograms recorded by the georods along the longitudinal profile (modified from Picotti et al., 2015). The vertical component is shown in (a), while the horizontal transverse component is shown in (b). To acquire the two components, the georods were rotated along the corresponding mutually perpendicular axes. The P and SH diving-wave first breaks are indicated.

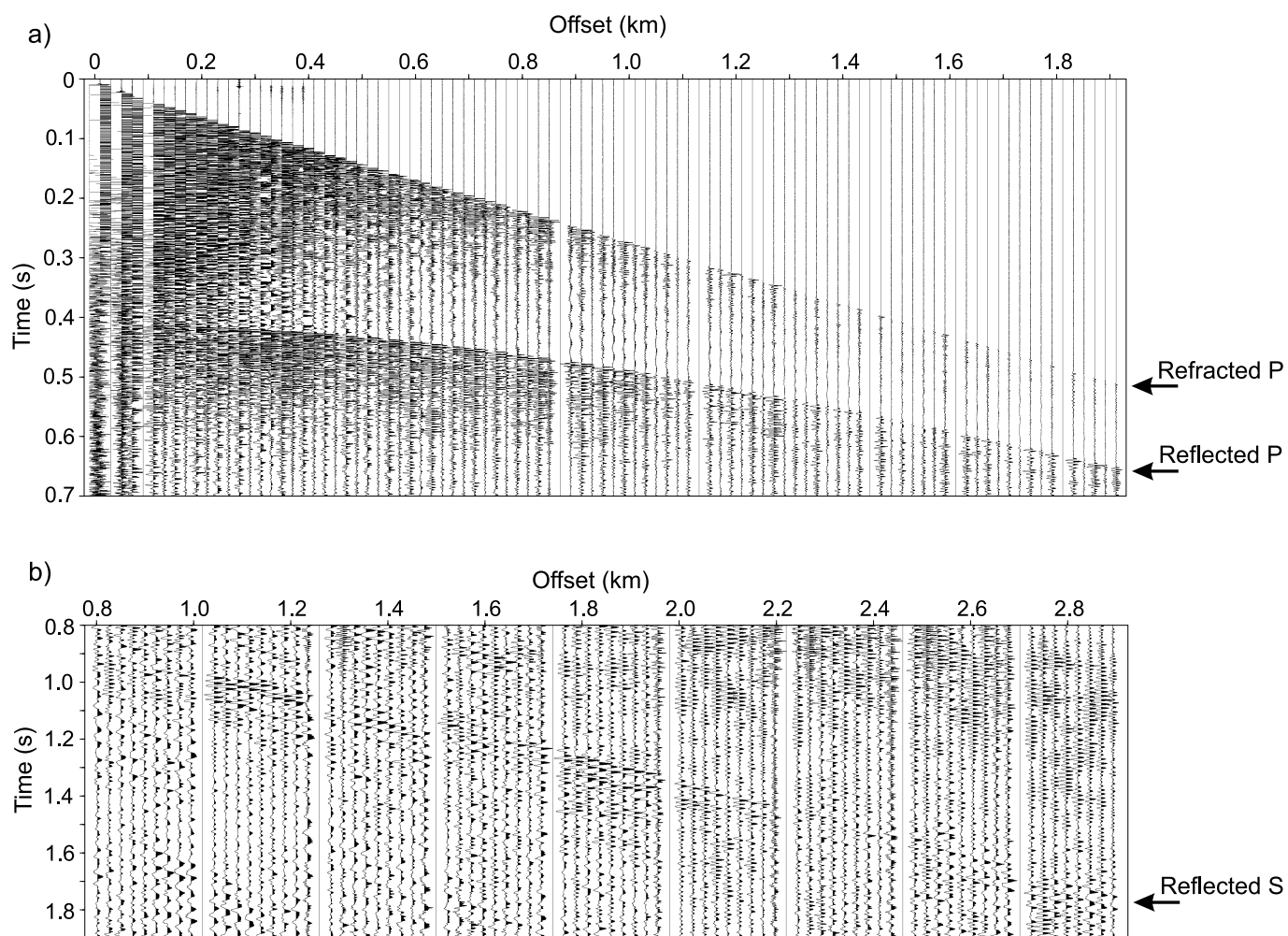


**Figure 3.** Explosive-charge seismograms recorded by the vertically-oriented geophones and georods (a), and by the 3C stations on the horizontal transverse component (modified from Picotti et al., 2015) (b). A 10-400 Hz band-pass filter is applied to remove the surface waves. The P and S waves reflected at the ice-sediments interface, as well as the P waves refracted at the bottom of the firm layer, are indicated.

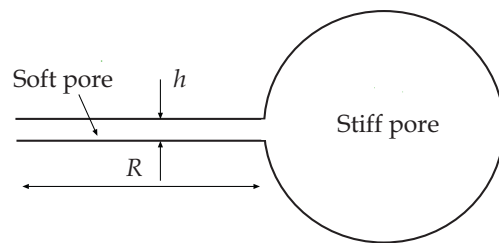


**Figure 4.** Sketch of the squirt-flow model, where two sandstone grains in contact are shown. The soft pores are the grain contacts and the stiff pores constitute the main porosity. The quantity  $R$  is the radius of the disk-shaped soft pore (half disk is represented in the plot).

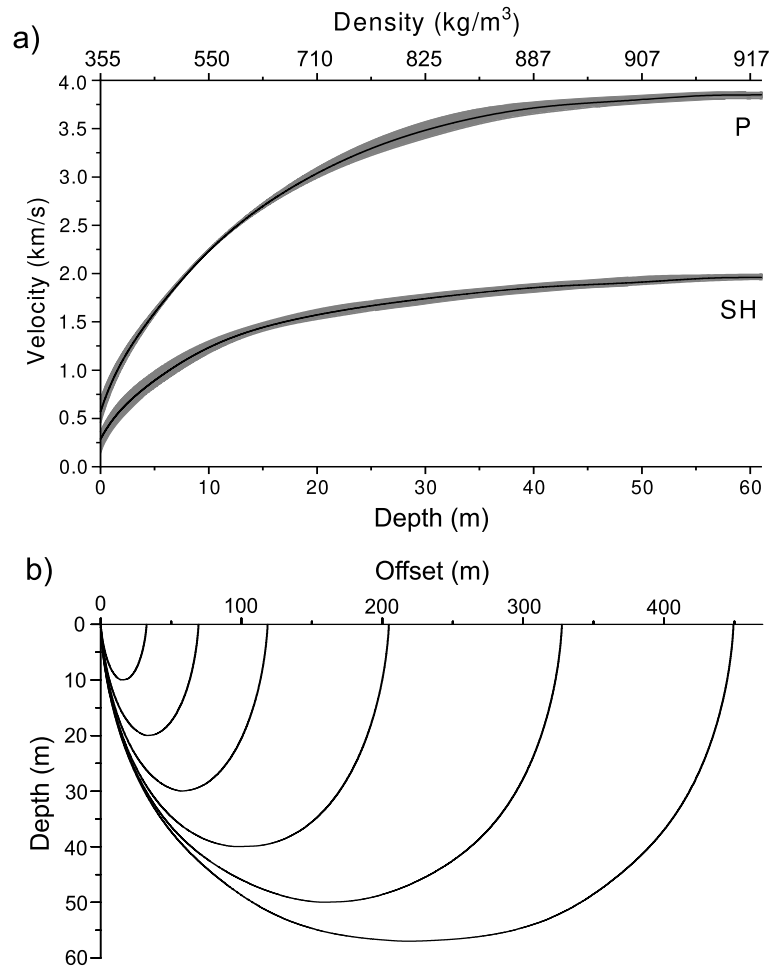


**Figure 5.** P- and S-wave velocity profiles as a function of depth obtained by using the Hergloz-Wiechert traveltimes inversion method, where the error in velocity is displayed as gray bands (a), and P-wave diving waves corresponding to some picked first-breaks (b). These plots are an improved version of those originally presented in Picotti et al. (2015). The velocity curves are also represented as a function of density using Eq. (13) proposed by Kohlen (1972).

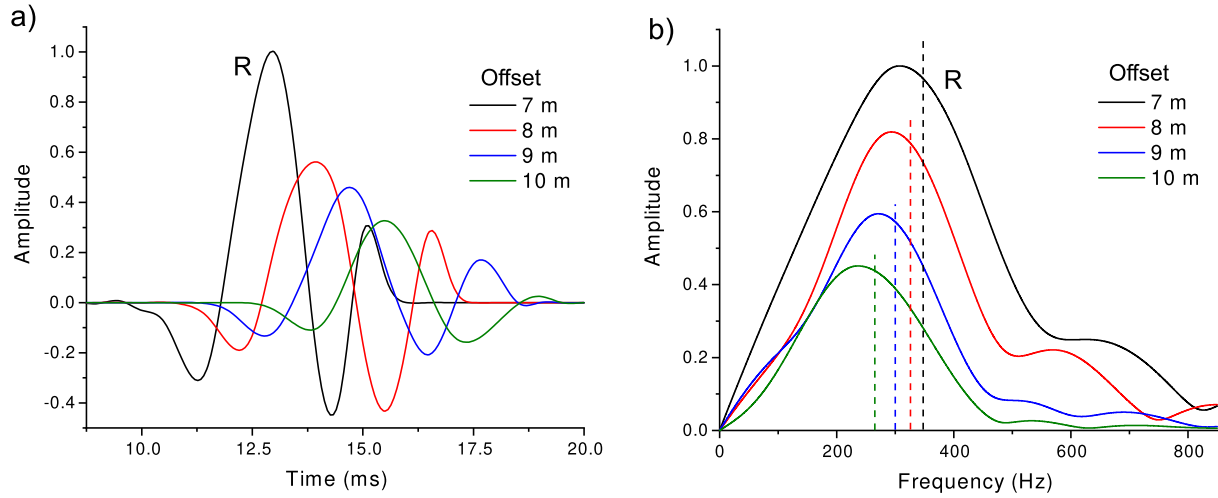


**Figure 6.** Time histories (a) and corresponding spectra (b) of the P-wave first breaks recorded between 7 and 10 m. The label *R* indicates the reference signal recorded at 7 m offset, while the vertical dashed lines indicate the frequency centroids.

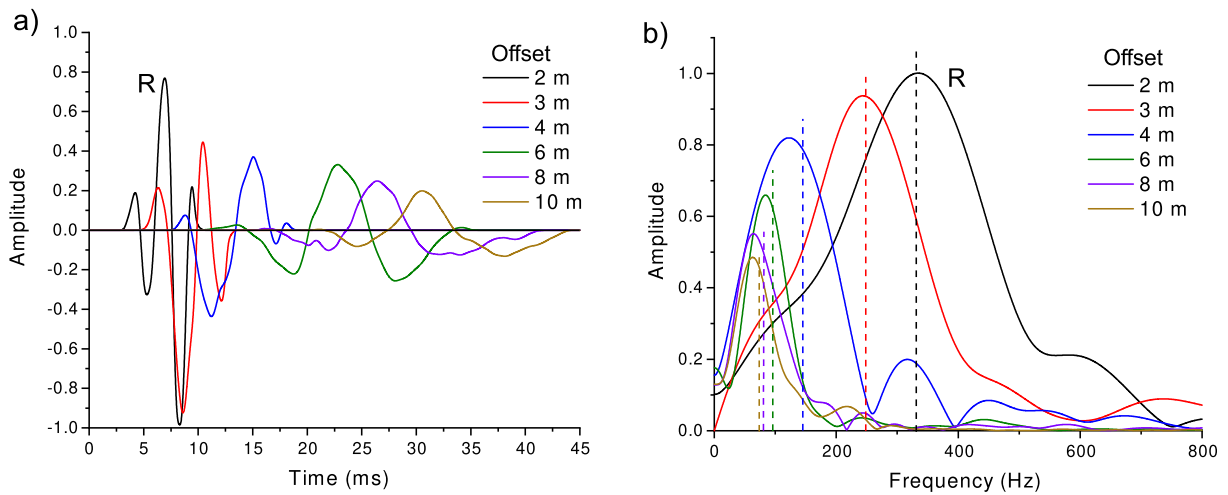


**Figure 7.** Time histories (a) and corresponding spectra (b) of the S-wave first breaks recorded between 2 and 10 m. The label *R* indicates the reference signal recorded at 2 m offset, while the vertical dashed lines indicate the frequency centroids.

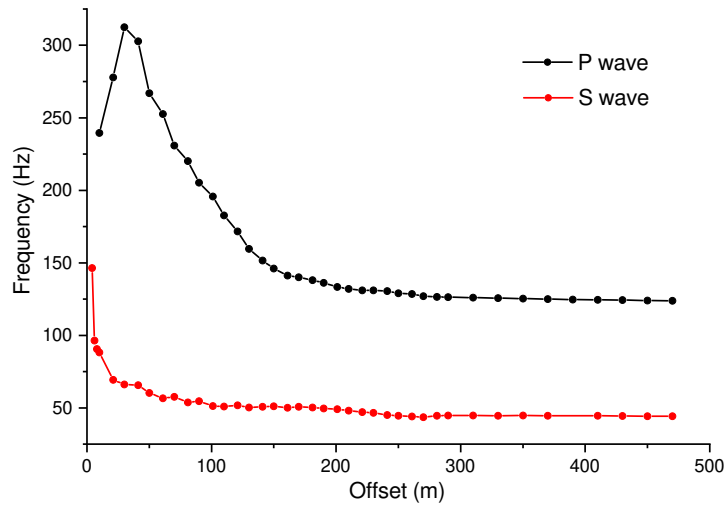


**Figure 8.** Dominant frequency of the diving P-wave (a) and S-wave (b) first-breaks as a function of offset.

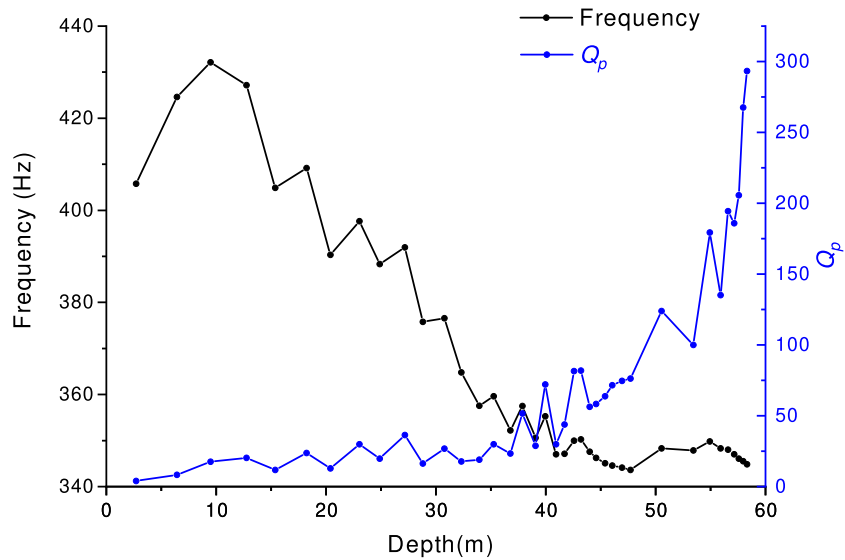


**Figure 9.** P-wave quality factor and dominant frequency as a function of depth, obtained from the layer-stripping frequency-shift method.



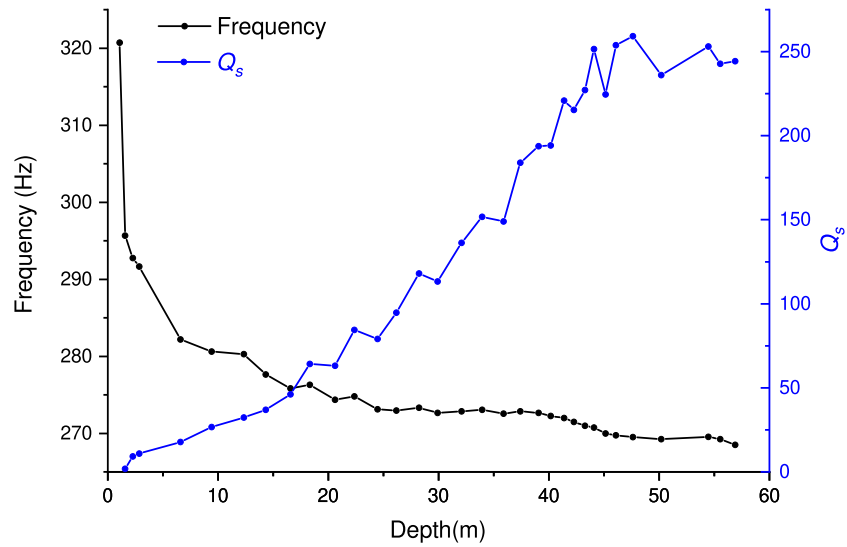


**Figure 10.** S-wave quality factor and dominant frequency as a function of depth, obtained from the layer-stripping frequency-shift method.

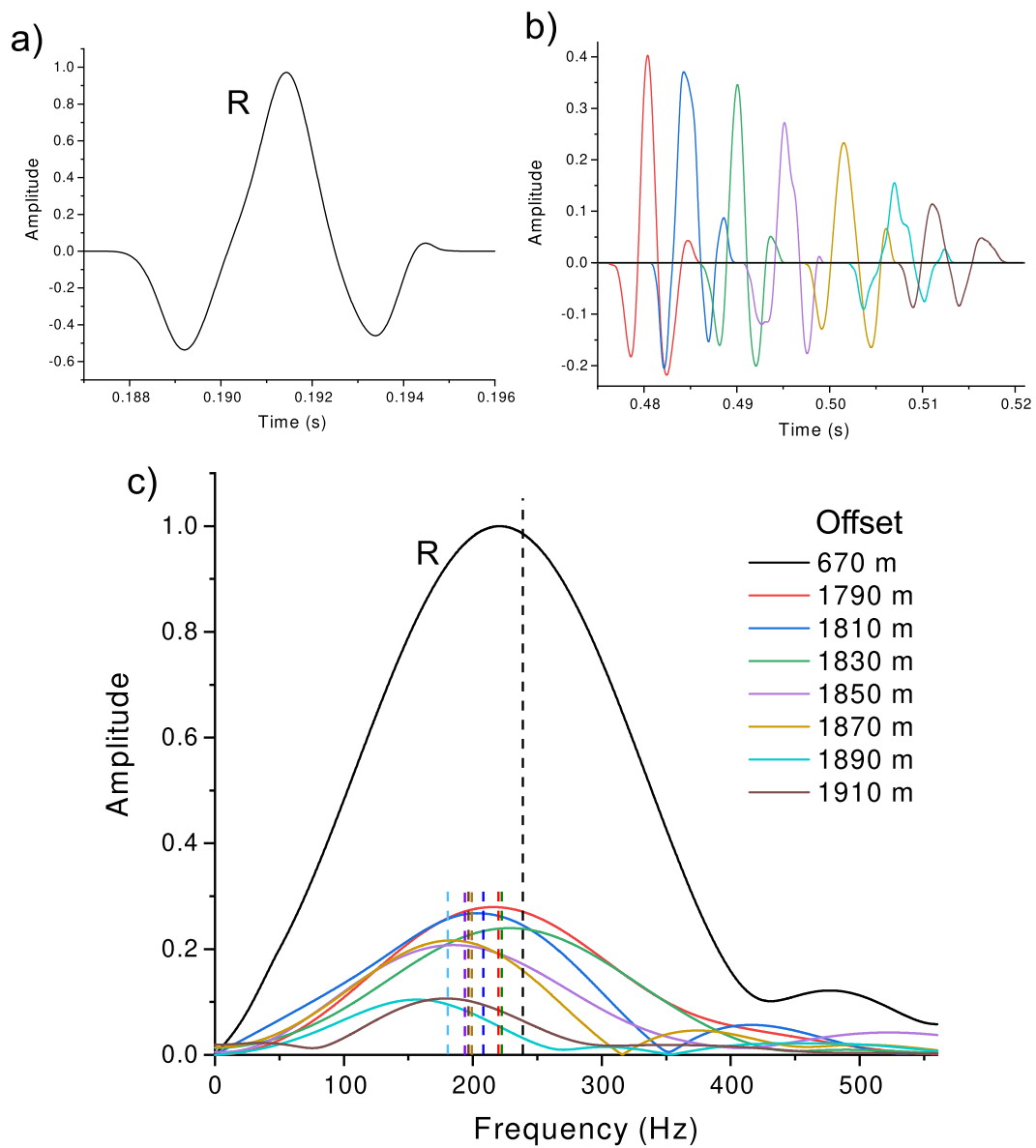


**Figure 11.** Time histories (b) and corresponding spectra (c) of the P-wave first breaks recorded at long offsets, between 1790 and 1910 m. The label *R* indicates the reference signal (a) recorded at 670 m offset, while the vertical dashed lines indicate the frequency centroids.

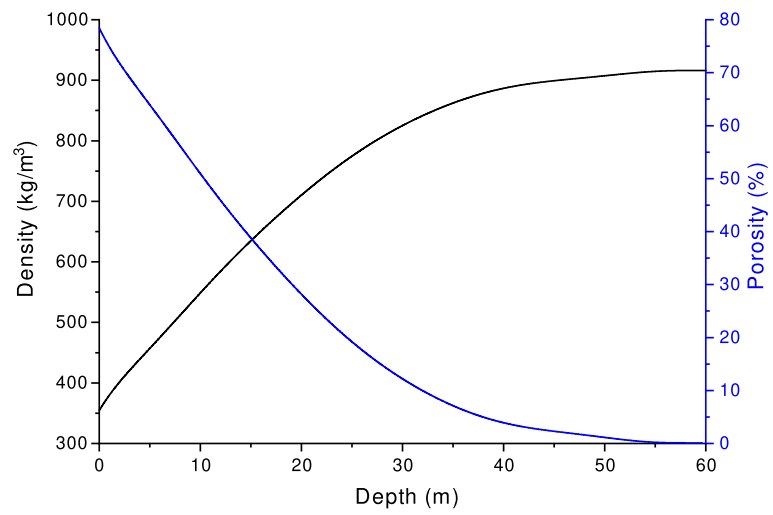


**Figure 12.** Density (black) and porosity (blue) as a function of depth.

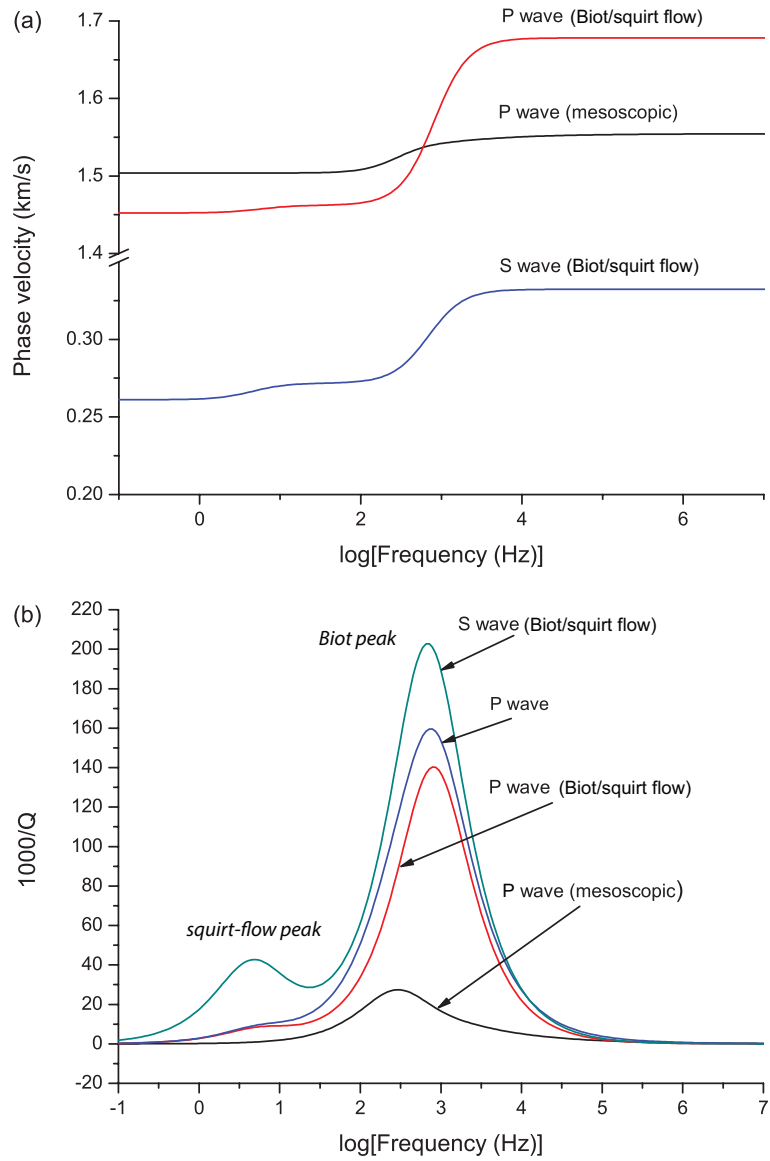


**Figure 13.** Analytical P-wave velocity (a) and dissipation factor (b) as a function of frequency, close to the surface.

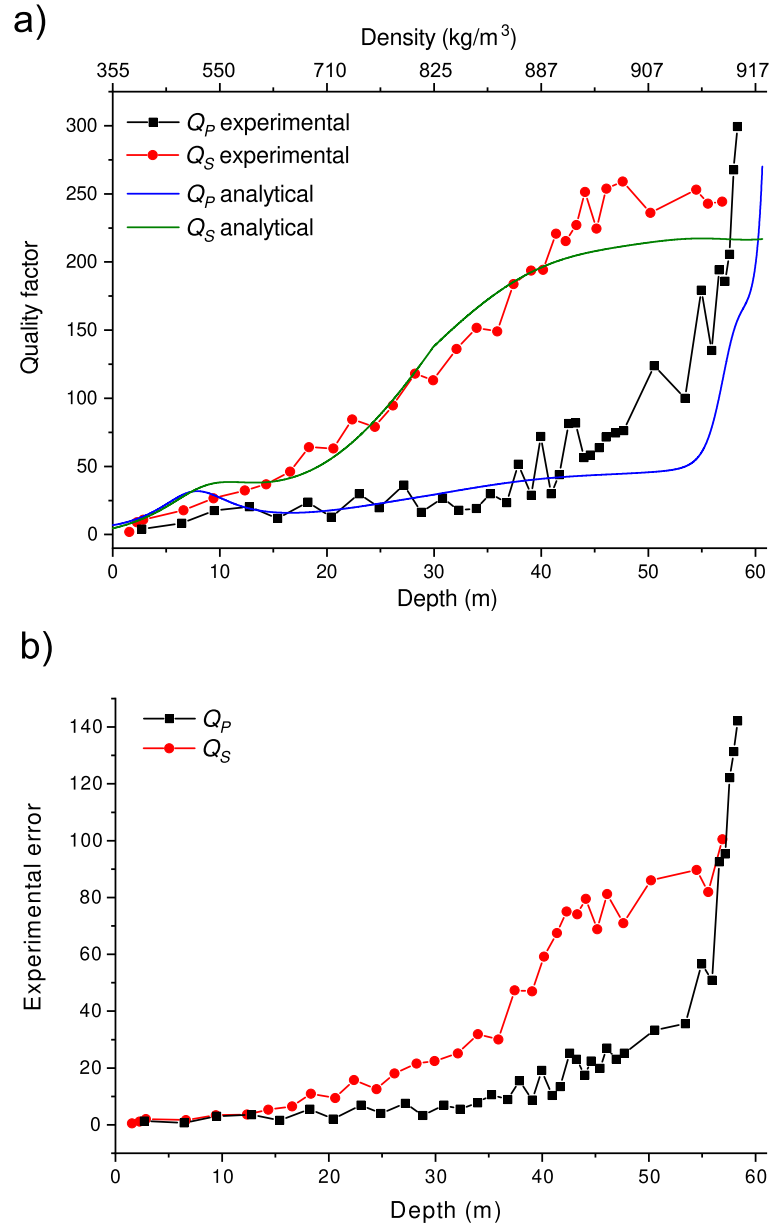


**Figure 14.** Comparison between the experimental (symbols) and theoretical (solid lines) P- and S-wave quality factors (a) as a function of depth. The quality factors are also represented as a function of density using Eq. (13) proposed by Kohnen (1972). Experimental errors (b) in the computation of  $Q_P$  and  $Q_S$  using the layer-stripping frequency-shift method.

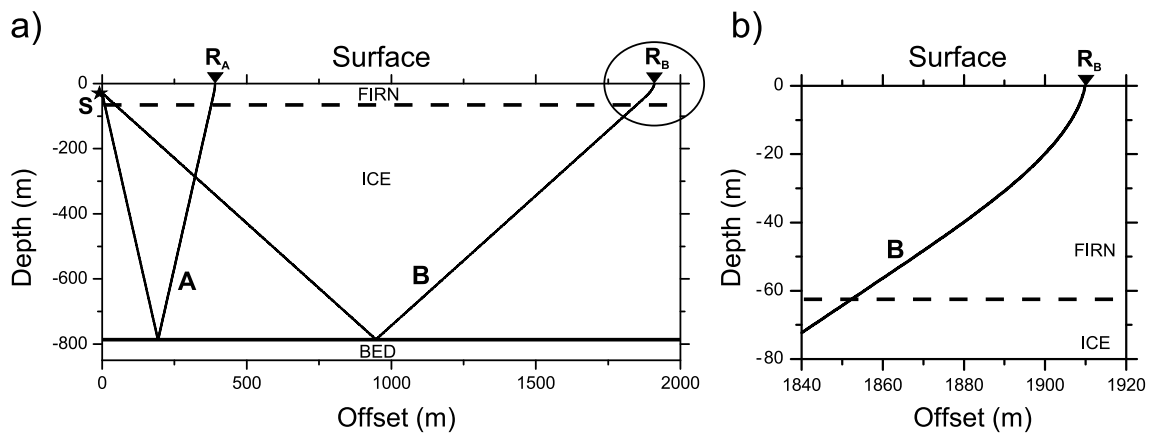


**Figure 15.** Ray tracing of P waves reflected from bed and emerging at approximately 390 m (ray A - reference wavelet) and 1910 m offset (ray B), respectively (a). Magnification of the P-wave ray emerging at the surface (b), in the area highlighted by the circle in (a), showing the deflection caused by the velocity gradient in the firn. The source (S), an explosive charge placed at a depth of 27 m, and the receivers ( $R_A$  and  $R_B$ ) are indicated. The surface and ice-bottom interface are almost flat, with slopes less than  $1^\circ$

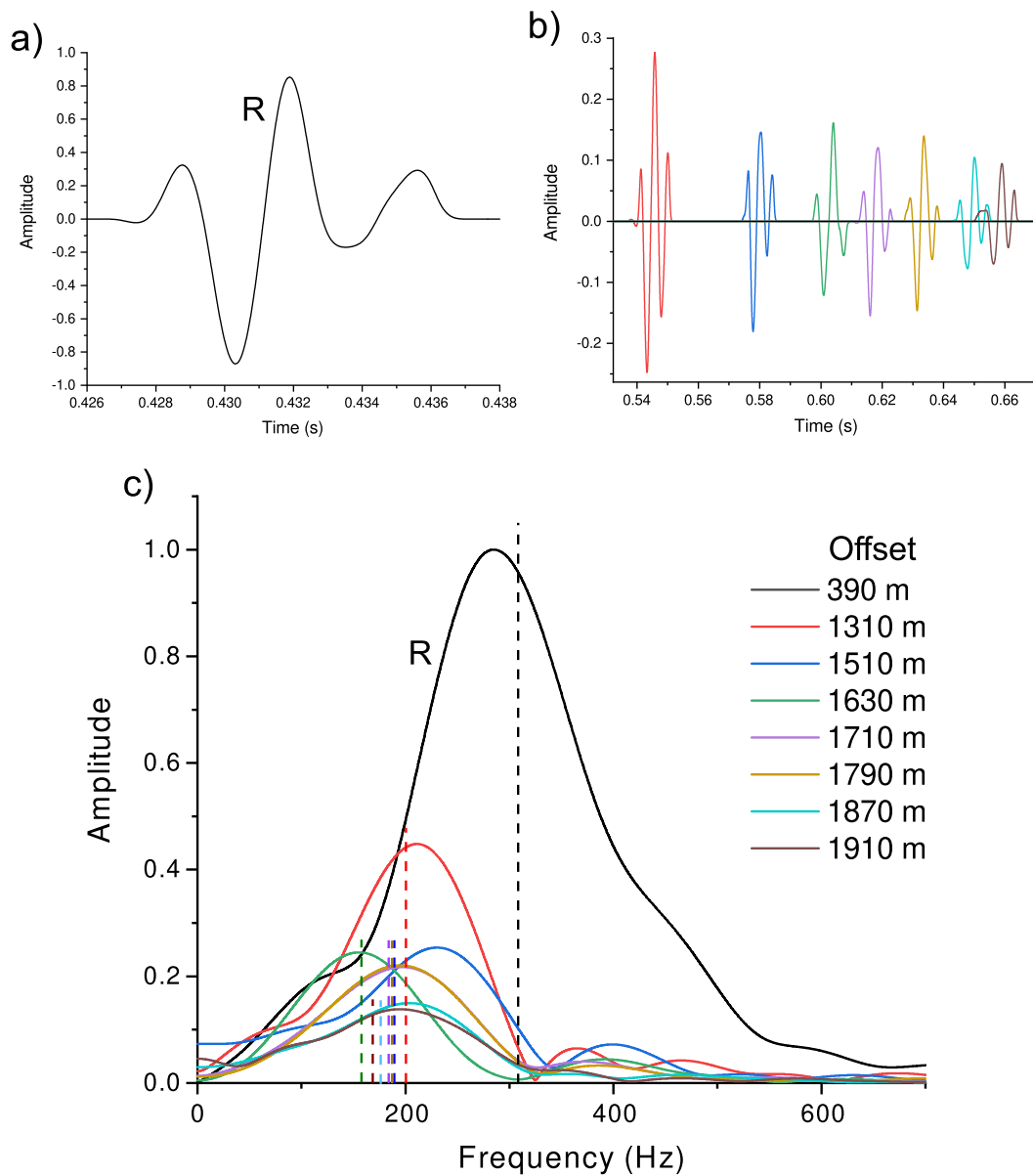


**Figure 16.** Time histories (b) and corresponding spectra (c) of the P-wave reflected wavelets recorded at long offsets, between 1310 and 1910 m. The label *R* indicates the reference signal (a) recorded at 390 m offset, while the vertical dashed lines indicate the frequency centroids.

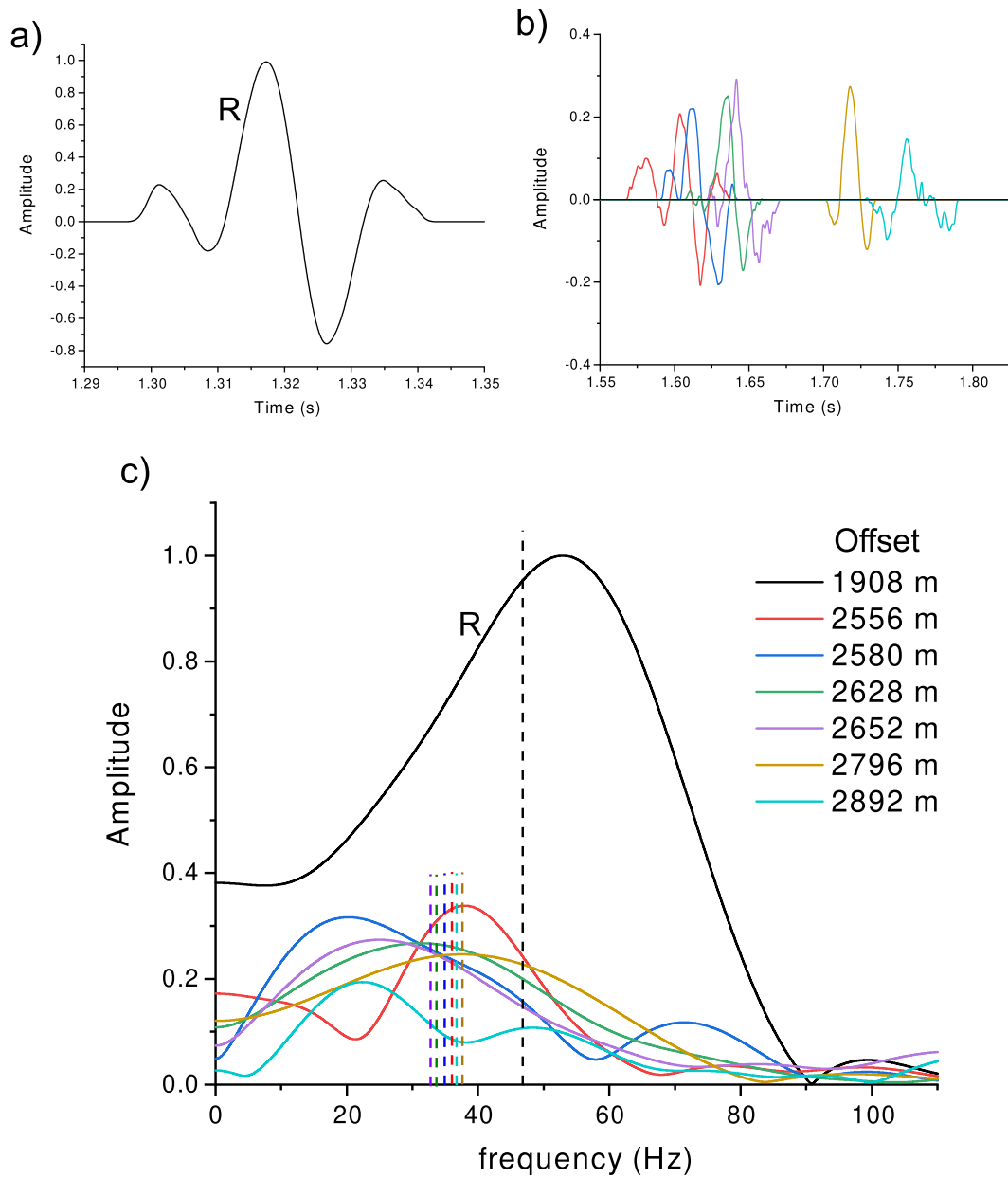


**Figure 17.** Time histories (b) and corresponding spectra (c) of the S-wave reflected wavelets recorded at long offsets, between 2556 and 2892 m. The label *R* indicates the reference signal (a) recorded at 1908 m offset, while the vertical dashed lines indicate the frequency centroids.